https://dx.doi.org/10.1016/j.watres.2018.10.094

Formation and Stability of NOM-Mn(III) Colloids in Aquatic Environments

Qianqian Li[a], Lin Xie[b], Yi Jiang[c], John D. Fortner[d], Kai Yu[a], Peng Liao[*,a], Chongxuan Liu[*,a]

[a]School of Environmental Science and Engineering, Guangdong Provincial Key Laboratory of Soil and Groundwater Pollution Control, Southern University of Science and Technology, 1088 Xueyuan Road, Shenzhen, 518055, P. R. China

[b]Department of Physics, Southern University of Science and Technology, 1088 Xueyuan Road, Shenzhen, 518055, P. R. China

[c]Department of Civil and Environmental Engineering, The Hong Kong Polytechnic University, Hung Hom, Kowloon, Hong Kong, China

[d]Department of Energy, Environmental and Chemical Engineering, Washington University in St. Louis, St. Louis, MO, USA

*Corresponding authors:

Peng Liao
liaop@sustc.edu.cn

Chongxuan Liu
liucx@sustc.edu.cn

Abstract

Soluble Mn(III) species stabilized by natural organic matter (NOM) plays a crucial role in a number of biogeochemical processes. To date, current understanding of these phenomena has been primarily concerned on the occurrence and chemistry of soluble NOM-Mn(III) complexes; much less is known regarding the formation and stability of NOM-Mn(III) colloids in the environment. This presents a critical knowledge gap with regard to biogeochemical cycling of manganese and associated carbon, and for predicting the fate and transport of colloid-associated contaminants, nutrients, and trace metals. In this work, we have characterized the chemical and physical properties of humic acid based (HA)-Mn(III) colloids formed over a range of environmentally relevant conditions and quantified their subsequent aggregation and stability behaviors. Results show that molar C/Mn ratios and HA types (Aldrich HA (AHA) and Pahokee peat soil HA (PPSHA)) are critical factors influencing HA-Mn(III) colloidal properties. Both the amount and the stability of HA-Mn(III) colloids increased with increasing initial molar C/Mn ratios, regardless of HA type. The correlation between the critical coagulation concentration (CCC) and zeta potential (R^2 > 0.97) suggests that both Derjaguin-Landau-Verwey-Overbeek (DLVO) type and non-DLVO interactions are responsible for enhanced stability of HA-Mn(III) colloids. For a given C/Mn ratio, PPSHA-Mn(III) colloids are significantly more stable against aggregation than AHA-Mn(III) colloids, which is likely due to stronger electrostatic interactions, hydration interactions, and steric hindrance. Further examination in real-world waters indicates that the HA-Mn(III) colloids are highly stable in surface river water, but become unstable (i.e. extensive aggregation) in solutions representing a groundwater-seawater interaction zone.

Overall, this study provides new insights into the formation and stability of NOM-Mn(III) colloids which are critical for understanding Mn-based colloidal behavior(s) , and thus Mn cycling processes, in aquatic systems.

Keywords: NOM-Mn(III) colloids, C/Mn ratios, HA types, colloid formation, colloid stability

1. Introduction

Manganese (Mn) is a redox active metal that occurs in various geological and environmental settings and can partake in a broad range of biogeochemical processes (Sunda et al., 1994; Post, 1999; Johnson, 2006; Madison et al., 2013; Gude et al., 2017). Traditionally, Mn is considered to be predominantly present as soluble Mn(II) in anoxic and in particulate form (Mn(IV/III)) in oxic environments (Stumm and Morgan, 1996). Dissolved Mn(III) in natural waters has been largely understudied as it is thermodynamically unstable and rapidly disproportionate to Mn(II) and Mn(IV) (Stumm and Morgan, 1996). However, molecular orbital theory has substantiated that the donating and accepting orbitals of Mn(II) and Mn(IV) are spatially distinct, indicating that Mn(II) oxidation and Mn(IV) reduction should proceed via a one-electron transfer, with Mn(III) as the intermediate (Luther, 2005). Consequently, Mn(III) can be isolated and stabilized in aqueous solutions under appropriate conditions.

Mounting field evidences highlight the prevalence of dissolved Mn(III) bound to a variety of organic ligands (e.g., humic substances, Mn(III)-L complexes) in aqueous systems (Trouwborst et al., 2006; Oldham, 2017). Recent studies demonstrated that: (1) Mn(III)-L complexes can constitute the majority of the total dissolved Mn pool in anoxic, suboxic, and oxic environments in oceans and estuary sediments, and (2) these species

can serve as both oxidant and reductant, and thus have important roles in the coupled cycles of carbon, iron, and sulfur (Trouwborst et al., 2006; Madison et al., 2013; Oldham et al., 2017a; Oldham, 2017). The formation of Mn(III)-L complexes has been proposed to occur through a sequence of reaction pathways that include oxidation, reduction, and ligand-promoted dissolution of Mn-bearing minerals (Madison et al., 2013; Oldham, 2017). In additional to natural systems, Mn(III)-L complexes can also form in situ during oxidative water treatment using Mn(VII) chemicals (Sun et al., 2015; Zhang et al., 2018). Resulting Mn(III)-L complexes have been verified to be strong oxidants and can contribute to the transformation of anthropogenic contaminants (Sun et al., 2015; Hu et al., 2017; Gao et al., 2018).

In addition to dissolved species, organic Mn(III)-L complexes also exist as colloids. Oldham (2017) documented that Mn(III) has a strong affinity with natural organic matter (NOM) such as humic substances. Although these humic-type Mn(III)-L complexes were identified to be largely non-colloidal (operationally defined as size class between 20 to 200 nm), Oldham et al. (2017b) speculated that a minor fraction of Mn(III)-humic complexes do exist as colloids. As colloids are broadly defined as dispersed particles with sizes between 1 nm and 1000 nm in diameter (Elimelech et al., 1995), the amount of dissolved Mn(III)-L complexes estimated using the previous definition (≤ 200–450 nm) should include both truly soluble (e.g., < 1–20 nm) and colloidal-based Mn(III). A recent study provided a compelling evidence that Mn(III)-L complexes in ocean exist both in colloidal form (20–400 nm) and truly dissolved form (< 20 nm), with colloids constituting up to 90% of the total Mn(III) (Yakushev, 2013).

In contrast to a growing body of studies pertaining to dissolved Mn(III) associated with NOM, little is known about the properties and behaviors of NOM-Mn(III) colloids in aquatic environments. This is likely due to the fact that the researchers have traditionally used filters of 0.2 μm or 0.45 μm pore size to separate samples into 'dissolved' and 'particulate' phases (Wu et al., 2001; Oldham, 2017). Further, results from previous field and laboratory studies indicate that the colloidal phase of NOM-metals (e.g., Fe) complexes can act as mobile carriers, facilitating the transport of low solubility contaminants at rates and distances much greater than the soluble phase of NOM-metals (Pokrovsky and Schott, 2002; Fannun, 2014). This warrants further studies to elucidate the formation, properties, and subsequent behaviors (e.g., aggregation) of NOM-Mn(III) colloids in an effort to accurately elucidate their fate and even potential as vectors in sequestrating and mobilizing contaminants. Additionally, aggregation behavior of NOM-Mn(III) colloids may significantly affect their reactivity and mass flux as well as the fate and transport of priority contaminants. It has also demonstrated that the ratio of NOM to metal is an important factor influencing the formation and stability of NOM-metals colloids (Liao et al., 2017a; Mensch et al., 2017). Previous studies suggest that NOM from different sources has distinct effects on the colloidal behaviors of carbon-based colloids (Jiang et al., 2017). Although the role of NOM on the aggregation of engineered Mn(IV) colloids has been evaluated (Huangfu et al., 2013), the aggregation of naturally formed NOM-Mn(III) colloids has not been specifically evaluated.

The objectives of this study are to provide new insights into the formation (e.g., concentration and properties) and stability (i.e. aggregation) of NOM-Mn(III) colloids in aqueous environments (see Table 1). The central hypothesis in this study is that the molar

ratio of C/Mn and different types of NOM can significantly affect the formation and aggregation of NOM-Mn(III) colloids. To test this, NOM-Mn(III) colloids were generated in batch experiments over a range of environmentally relevant C/Mn ratios with different NOM types, and those colloids and their aggregation behaviors were subsequently characterized using a suite of complementary characterization techniques. The stability of the formed NOM-Mn(III) colloids in real river and groundwater were also examined. Findings add a perspective to understanding of the stability of NOM-Mn(III) colloids and the ability to quantitatively predict the fate of contaminants, nutrients, and trace metals associated with NOM-Mn(III) colloids in aquatic environments.

2. Materials and methods

2.1. Materials

All reagent solutions were prepared using ultrapure water (resistivity >18.2 MΩ·cm, Milli-Q, Millipore). A stock solution of Mn(III) was prepared by dissolving 0.0134 g of manganese-(III) acetate dihydrate (>97%, Alfa Aesar) solid in 500 mL water to reach a concentration of 100 μM. Two sources of humic acid (HA), one from Aldrich HA (AHA, Sigma Aldrich) and the other extracted from Pahokee (Florida) peat soils (PPSHA, 2BS103P, International Humic Substances Society (IHSS)), which have been extensively used in previous studies (Meyer et al., 2015; Liao et al., 2017a,b; Jiang et al., 2017), were selected as model NOM compounds in this study. Both HA stock solutions were prepared by introducing 2.5 g of the dry HA power in 500 mL water and adjusting pH to 10.5 using 1 M NaOH. The mixture was allowed to stir on a magnetic stirrer for 24 h in the dark and the resulting solution was filtered through 0.45 μm nitrocellulose filters

(Millipore). The total organic carbon (TOC) in the AHA and PPSHA stock suspensions was determined to be 1661 ± 7 and 1715 ± 16 mg C/L, respectively, using a TOC analyzer (Multi N/C 3100, Analytik Jena, Germany). Specific UV absorbance ($SUVA_{254}$) for both HAs were determined by diluting HAs stock solutions to different concentrations (i.e., 1−10 mg C/L) and measure their UV absorbance at 254 nm using a UV-vis spectrophotometer (Cary 60, Agilent). Both stock suspensions were then used to create suspensions with different working concentrations for subsequent experiments. The properties of the two HAs are summarized in Table 2.

2.2. Formation and Characterization of HA-Mn(III) colloids

Duplicate batch experiments were performed to evaluate the effects of molar C/Mn ratios and HA types on HA-Mn(III) colloids formation. All reactions took place under oxic conditions in capped and stirred glass reactors (50 mL) that were shielded with aluminum foil to prevent photochemical reactions of Mn that may generate reactive oxygen species. The solutions in all the reactors were maintained at pH 7.0 using NaOH and/or HCl. NOM-Mn(III) colloids formation experiment was initiated by mixing aliquots of fresh Mn(III) stock solution with an array of HA (AHA and PPSHA) working suspensions at concentrations ranging from 0 to 30 mg C/L with a final Mn(III) concentration of 50 μM and molar C/Mn ratios of 0−50. These molar ratios were chosen because they cover a range of C/Mn molar ratios typically observed in sediments and tidal rivers. The suspensions were equilibrated under a stir condition (600 rpm) for 12 h at room temperature. Duplicate control experiments were performed in parallel using HA suspension alone. Samples from different reactors at the termination of the experiments

were collected for chemical analysis, characterization, and for subsequent aggregation experiments described in the next section.

The concentrations of Mn and HA in different size fractions were first quantified by wet chemical analysis. Colloids defined in this study as particles ranging from 10000 Da (roughly equal to 1−3 nm) to 0.45 μm. Sample passed through the 10000 Da ultrafiltration membrane was defined as truly soluble and that retained on the 0.45 μm filter was defined as particulate species. The fractions of Mn and HA in truly dissolved species (roughly equal to < 1−3 nm), colloids (< 1−3 to 450 nm), and particulates (> 450 nm) were operationally separated from samples by 10000 Da ultrafiltration membranes (EMD, Millipore) and 0.45 μm filters (PES, Whatman). Total Mn concentration in each fraction was determined by inductively coupled plasma mass spectrometry (ICP-MS) (Agilent 7700 series) after acidification of the samples with 2% HNO_3. Although the ICP-MS could not differentiate the valence of Mn, our X-ray photoelectron spectroscopy (XPS) results shown below confirmed Mn(III) dominated. The HA concentration in each fraction was quantified by a TOC analyzer described above.

The surface properties and crystalline nature of HA-Mn colloids were characterized using Fourier transform infrared (FTIR), XPS, and powder X-ray diffraction (XRD). Solid samples were obtained by ultracentrifugation followed by freeze-drying. FTIR spectra were recorded using a diffuse reflectance accessory coupled to a Nicolet iS 50 FTIR instrument (Thermo). Samples were mixed with KBr powder at a 1:10 ratio in an agate mortar and pestle. A KBr background spectrum was collected for subtraction before collecting the sample spectrum. XPS spectra were collected using a PHI Quantera SXM scanning X-ray microprobe with an Al mono source. The analyses were conducted at 26

187 eV pass energy at a 200 μm X-ray spot size. Calibration was performed by alignment of
188 the spectra with reference to the C 1s at 284.8 eV associated with graphitic carbon.
189 Powder XRD was collected in a Bruker D8 Advance X-ray diffractometer using Cu Kα
190 radiation.

191 Size distributions of HA-Mn suspensions were determined by dynamic light
192 scattering (DLS) using a Zetasizer Nano (Malvern, UK). Measurements were also made
193 to monitor the electrophoretic mobility, which was subsequently converted to zeta
194 potential using the Smoluchowski approximation (Elimelech et al., 1995). For each
195 measurement, approximately 1 mL of the suspension was added into a polystyrene
196 cuvette and analyzed immediately.

197 The structure and morphology of HA-Mn colloids were determined by a
198 double-spherical aberration-corrected scanning transmission electron microscope
199 (Cs-corrected STEM, Thermo Fisher, Titan Themis G2 60-300) operating at 300 kV and
200 equipped with a high brightness X-FEG Schottky field emission gun and four Super-X
201 silicon drift X-ray energy-dispersive spectroscopy (EDS) detectors that can produce
202 ultrahigh X-ray count rates for elemental identification on a sub-nano or atomic scale.
203 The imaging was performed in STEM mode using high angle annular dark field
204 (HAADF) detector. Samples were prepared by placing ~ 20 μL of HA-Mn suspension
205 onto both side of a 10 nm thick windows of silicon nitride (SiN) membrane (SN100,
206 SiMPore Inc, USA) with the aim to obtain high-resolution microscopy images and
207 eliminate the interference of background carbon in collecting the elemental mapping of
208 HA-Mn colloids. The water remaining in the SiN window was immediately evaporated at
209 room temperature under vacuum.

2.3. Aggregation of HA-Mn(III) colloids

Time-resolved DLS was used to evaluate the aggregation kinetics of formed NOM-Mn(III) colloids by monitoring their early stage of Z-averaged hydrodynamic diameter with time over a wide range of electrolyte concentrations. HA-Mn(III) colloids were separated by successive fractionation of the equilibrated samples with different molar C/Mn ratios using 10 kDa ultrafiltration and 0.45 μm filters as described above. The resulting HA-Mn(III) colloids obtained under all conditions (different C/Mn ratios and different HA types) are visually stable (Fig. S2). Because negligible aggregation of HA-Mn(III) colloids was observed for high monovalent cation concentrations (i.e., 1000 mM NaCl, Fig. S3), we devote our consideration of aggregation as a function of divalent cations. The aggregation kinetics of HA-Mn(III) colloids were initiated by introducing an electrolyte with a divalent cation (Ca^{2+} and Mg^{2+}) that induced aggregation. Ca^{2+} and Mg^{2+} were selected as they are naturally abundant and are widely used in prior studies as representative divalent cations for particle aggregation (Chen et al., 2006; Philippe and Schaumann, 2014; Li et al., 2014; Jiang et al., 2016; Xu et al., 2017). For each measurement, an appropriate volume of HA-Mn(III) colloids suspension (~ 1 mL) at a given molar C/Mn ratio was pipetted into a cuvette. Subsequently, a pre-determined amount of electrolyte stock solution was quickly transferred into the cuvette to obtain a desired electrolyte concentration. The cuvette (a total volume of 1 mL) was vigorously vortexed before being inserted into the DLS chamber immediately after. The initial change in the average hydrodynamic diameter (D_h) was monitored every 15 s over a time period of 20 min. Control experiments with HA alone (10 mg C/L) were performed with the same procedures and range of electrolyte concentrations.

The early state aggregation rate constant of HA-Mn(III) colloids (k) was acquired by measuring the increase in D_h with time (t).

$$k \propto \frac{1}{N_0}\left(\frac{dD_h(t)}{dt}\right)_{t\to 0} \quad (1)$$

where N_0 is the initial particle concentration in the suspension. The initial slope, $dD_h(t)_{t\to 0}$, was calculated from a linear least-squares regression analysis of the increase in D_h up to the point where $dD_h(t)$ reaches 1.5 $dD_h(0)$. The aggregation attachment efficiency (α), which is the inverse stability ratio that ranges from 0 to 1, was calculated by normalizing the initial aggregation rate constant obtained at a given electrolyte concentration (k) to that under diffusion-limited (nonrepulsive, fast) aggregation conditions (k_{fast}). Given that N_0 was kept constant throughout each aggregation experiment, α can be determined as the ratio of the initial slope obtained in the reaction limited regime to that in the diffusion-limited regime.

$$\alpha = \frac{k}{k_{fast}} = \frac{\frac{1}{N_0}\left(\frac{d}{dt}D_h(t)\right)_{t\to 0}}{\frac{1}{N_{0,fast}}\left(\frac{d}{dt}D_h(t)\right)_{t\to 0,fast}} = \frac{\left(\frac{d}{dt}D_h(t)\right)_{t\to 0}}{\left(\frac{d}{dt}D_h(t)\right)_{t\to 0,fast}} \quad (2)$$

2.4. Stability of HA-Mn(III) colloids in natural waters

Natural surface water was collected from Maozhou River, a contaminated tidal river in Pearl River delta, southern China (N22°44′46.85′′ E113°46′05.67′′). Natural groundwater (−18 m depth) was collected from a groundwater-seawater interaction zone that is in close proximity to the Maozhou River (N22°47′38.51′′ E113°49′28.43′′). The resulting groundwater was mixed with DI water in different proportions to generate a set of solutions with different salinity. The detailed locations for surface and groundwater sampling points is displayed in Fig S1. Detailed sampling and characterization of the water samples can be found in Supplementary Material and a summary of water

chemistry composition is provided in Table S1. The stability of HA-Mn(III) colloids was measured by dispersing HA-Mn(III) colloids (both for AHA-Mn(III) and PPSHA-Mn(III) with the same molar C/Mn ratio of 50) in each solutions and then monitoring size changes over time via TR-DLS. Measurements were taken every 20 s for 1 h.

3. Results and Discussion

3.1. Formation of NOM-Mn(III) colloids

Concentration distributions of Mn in HA-Mn(III) suspensions, under steady-state conditions, show that the colloidal fraction of Mn(III) (1-3 ~ 450 nm) increases with increasing initial molar C/Mn ratio (Fig. 1a,b). No colloidal Mn(III) was observed in the absence of HA (C/Mn = 0). For both AHA and PPSHA, the colloidal Mn(III) concentration increased linearly with increasing initial molar C/Mn ratio from 0 to 10, followed by a progressive approach to a maximum (36.0% for AHA-Mn(III) and 43.0 for PPSHA-Mn(III)) with a further increase in C/Mn ratio to 50 (Fig. 1a,b). Truly soluble Mn(III) (< 1-3 nm) correspondingly dropped from 38% to 2.7% for AHA-Mn(III) suspension and to 3.5% for PPSHA-Mn(III) suspension. Given that the particulate Mn(III) (> 450 nm) did not substantially change with the change in C/Mn ratio (Fig. 1a,b), an increase in colloidal Mn(III) can readily be attributed to the decrease in truly soluble Mn(III).

Consistent with the changes of Mn(III) in different size fractions, the truly soluble HA diminished linearly from ~ 85 to ~20% as the initial C/Mn ratio increased from 2.5 to 50 with most of the increase in HA appearing in the colloidal fraction (Fig. 1c,d). This is in contrast to control results in the absence of Mn(III) whereby HA existed primarily in

colloidal forms over a range of HA concentrations (2.5-30 mg C/L) (Fig. 1e). Such discrepancy in HAs size distribution before and after reacting with Mn(III) is attributed to interactions between Mn(III) and HA. For instance, the sharp increase in truly soluble HA at lower initial molar C/Mn ratios (≤ 5.0) is likely due to the complexation of HA with truly soluble Mn(III) via ligand exchange mechanism (Oldham, 2017), which may lower the free fraction of colloidal HA. A qualitative distribution comparisons indicate that the complexation of truly soluble Mn(III) by HA and the subsequent coagulation of HA macromolecular particles were responsible for the formation of NOM-Mn(III) colloids. An excellent logarithmic correlation between the colloidal Mn(III) and colloidal HA further confirmed the colloidal association between Mn(III) and HA (Fig. S4).

To further quantitatively probe the association between Mn(III) and HA for HA-Mn(III) colloids formation, we evaluated the ratio of the average stability constants for Mn(III) bound by truly soluble HA to that of Mn(III) bound by colloidal HA ($K_{Mn(III)\text{-}Sol.HA}$/ $K_{Mn(III)\text{-}Coll.HA}$) (Fig. 1f) (Wu et al., 2001). The ratios of $K_{Mn(III)\text{-}Sol.HA}$/ $K_{Mn(III)\text{-}Coll.HA}$ were determined to be < 1.0 when the initial C/Mn molar ratio exceeds 5.0, suggesting that colloidal HA may have a higher affinity for associating Mn(III) than truly soluble HA. Additionally, the ratio of $K_{Mn(III)\text{-}Sol.HA}$/ $K_{Mn(III)\text{-}Coll.HA}$ for PPSHA systems is consistently lower than that for AHA systems, demonstrating that PPSHA has a higher preference for Mn(III) compared to AHA for HA-Mn(III) colloids formation. It is noteworthy that the colloidal molar C/Mn ratios (i.e. the ratio of HA and Mn concentrations in the colloidal fraction) are positively correlated with the initial molar C/Mn ratios for both HAs (R^2 = 0.998, Fig. S5). A slope of 2.0 suggests that HA-Mn(III) colloids accounted for ~ 50% of total HA-Mn(III) complexes. This is in contrast to our

304 recent study, showing that the majority (> 90%) of HA-Fe(III) complexes were colloids
305 until the initial molar C/Fe ratios exceeds 1.6 (Liao et al., 2017a).

306 Taken together, our findings indicate that the relative amount of HA-Mn(III) colloids
307 increased with increasing molar C/Mn ratios and that PPSHA has stronger association
308 with Mn(III) compared to AHA for HA-Mn(III) colloids formation. Further additional
309 evidence supporting this conclusion is provided by complementary characterization data
310 presented below.

311

312 ***3.2. Characterization of NOM-Mn(III) colloids***

313 Resulting chemical properties of HA-Mn(III) colloids were determined using FTIR
314 spectroscopy (Fig. 2a). The FTIR spectra of HA-Mn(III) colloids are significantly
315 different from HAs prior to reaction. Compared to HA samples, a strong adsorption band
316 at 510 cm^{-1} appeared in HA-Mn(III) systems. This peak was attributed to the formation of
317 Mn^{3+}-O structure, as discussed by others (Julien et al., 2004). The asymmetric and
318 symmetric COO^- bands at 1595 and 1390 cm^{-1} in HA samples also become smaller and
319 shift to 1610 and 1400 cm^{-1} for HA-Mn(III) samples. Such a shift and change in the
320 shape of COO^- stretching bands is typically linked to the carboxylate-metal bond
321 formation (Sharma et al., 2010; Chen et al., 2014), thus suggesting that COO^- is likely the
322 main functional group of HA for associating with Mn(III), with respect to HA-Mn(III)
323 colloids formation. Similar observations have been reported for NOM-Fe(III) colloids
324 (Sharma et al., 2010). A comparison of the peak intensity at ~1400 cm^{-1} suggests that a
325 higher COO^- amount occurs in PPSHA-Mn(III) colloids relative to AHA-Mn(III) colloids
326 at comparable C/Mn ratio. The crystalline nature of the formed HA-Mn(III) was also

identified by powder XRD (Fig. 2b). XRD patterns of both AHA-Mn(III) and PPSHA-Mn(III) colloids formed at an initial molar C/Mn ratio of 50 showed no obvious characteristic peaks for Mn(III) oxides, indicative of poor crystallinity or amorphous materials.

Surface-sensitive XPS was further used to characterize surface properties of HA-Mn(III) colloids (Fig. 2c-f). The quantification of Mn valence state on the solid surface suggests that no redox reaction occurs between HA and Mn(III) throughout the experiments as the average oxidation state of Mn was determined to be 3.04 (Fig. 2c,d), which is close to 3.0 of Mn(III). The deconvoluted peaks of C 1s spectra shows that the carboxyl carbon amounts (e.g., O-C=O) for PPSHA-Mn(III) colloids was slightly higher than for AHA-Mn(III) colloids (Fig. 2e,f), coinciding with FTIR observations. It is worth noting that the surface molar C/Mn ratios detected by XPS were substantially higher than the colloidal molar C/Mn ratios and total molar C/Mn ratios (Table S2). This is likely a result of the uneven spatial distribution of HA in HA-Mn(III) colloids with the HA being enriched on the colloid surface. Similar observations have also been made regarding the relative enrichment of HA on the surfaces of NOM-Fe colloids (Oleinikova et al., 2017; Liao et al., 2017a).

The hydrodynamic diameter and zeta potential of formed HA-Mn(III) colloids were monitored at experimental termination to explore their stability (Fig. 3). Regardless of the molar C/Mn ratios and the types of HA, HA-Mn(III) bulk suspensions (without any filtration treatments) have a broad size distribution and their Z-averaged hydrodynamic diameter approaches to ~1200 nm (Fig. 3a), primarily due to the presence of larger portions of particulate Mn(III), suggesting a wide degree of aggregation. Sedimentation

experiments (i.e., 1 h duration) support these observations, showing that almost all aggregates settled out of suspension (Fig. S6). In contrast, HA-Mn(III) colloids displayed a monodisperse and relatively narrow size distribution with a Z-averaged hydrodynamic diameter in the range of 150-250 nm, which is similar to the size of HA alone in the control experiments (Fig. S7a). In contrast to the insignificant change in the zeta potential of HA alone at any concentration examined (Fig. S7b), the zeta potential of HA-Mn(III) colloids became progressively more negative as molar C/Mn ratios increased (Fig. 3b). Further, PPSHA-Mn(III) colloids possessed an overall more negative charge than AHA-Mn(III) colloids. This is primarily because of a relatively higher amount of deprotonated COO^- groups existing for PPSHA-Mn(III) colloids as discussed above.

Ultrahigh resolution aberration-corrected HAADF-STEM imaging was employed to gain insights into the morphology and microscopic structural features of HA-Mn(III) colloids (Fig. 4). For both HAs systems, HA-Mn(III) colloids predominantly exhibited clear thin thread- and ringlike structures (Fig. 4a-d) that are analogous to humic substances previously imaged in the presence of Fe(III) (Myneni et al., 1999). The average diameter of a single ring structure ranged from ~ 20 to 80 nm as determined from the high magnification HAADF images (Fig. 4c,d). Selected area electron diffraction (SAED) patterns showed poor crystallinity of both HA-Mn(III) colloids (Fig. S8a,d), which is consistent with the powder XRD observations (Fig. 2b). Atomic resolution TEM images and fast Fourier transform (FFT) of micro grains further confirm the poor crystallinity of HA-Mn(III) colloids (Fig. S8b,c,e,f). Because the intensity of HAADF-STEM imaging is approximately proportional to the atomic number and sample thickness (Pennycook, 2011), brighter portions in the HAADF images are expected to be

373 Mn(III) due to the fact that Mn has the largest atomic number (55) compared to oxygen
374 (8) and C (6). It is clear that Mn(III) was either homogenously or heterogeneously
375 distributed in the ringlike structures of HAs (Fig. 4c,d), further confirming the close
376 association of Mn(III) with HA through complexation. More detailed information
377 regarding the structure and distribution of HA-Mn(III) colloids can be gained from the
378 EDS mapping results (Fig. 4e,f), which showed that the intensity of Mn(III) and HA are
379 very well matched at the edge region of the ringlike structures.
380
381 ***3.3. Aggregation and stability of NOM-Mn(III) colloids***
382 The stability of NOM-Mn(III) colloids was evaluated using hydrodynamic diameter
383 growth data (Figs. S9), from which aggregation attachment efficiency was obtained over
384 a range of divalent electrolyte concentrations (Fig. 5). In both $CaCl_2$ and $MgCl_2$ solutions,
385 NOM-Mn(III) colloids formed at different C/Mn ratios and different HA types exhibited
386 distinct reaction-limited aggregation (RLA) and diffusion-limited aggregation (DLA)
387 regimes, suggesting that electrostatic Derjaguin-Landau-Verwey-Overbeek (DLVO) type
388 interactions were the main mechanism for stabilization (Saleh et al., 2008; Aich et al.,
389 2016). Similar observations have been reported for the aggregation of other
390 NOM-based/coated (metal) colloids or nanoparticles such as HA-Fe(II/III) colloids,
391 higher-order fullerene clusters, dissolved black carbon, diesel soot nanoparticles, and
392 graphene oxides (Aich et al., 2016; Chen and Huang, 2017; Jiang et al., 2017; Liao et al.,
393 2017a; Xu et al., 2017). Within the RLA at low electrolyte concentrations ($\alpha < 1$,
394 unfavorable), an increase in salt concentration screened the surface charge, as confirmed
395 by the electrokinetic measurements, showing that the zeta potentials of NOM-Mn(III)

colloids became less negative with increasing salt concentration (Fig. 6). This effectively diminished the electrostatic energy barrier for aggregation, thus leading to the increase in the rate of particle-particle attachment (efficiency). When the salt concentration exceeded the critical coagulation concentration (CCC), the repulsive energy barrier between particles is completely eliminated, resulting in DLA ($\alpha = 1$, favorable) and the changes of hydrodynamic diameter and attachment efficiency become independent of salt concentration (Figs. 5 and S9). As the minimum electrolyte concentration required to completely destabilize a stable colloidal suspension, CCC serves as an index to quantitatively evaluate and compare aqueous stability of colloidal particles; the higher CCC values led to the higher stability degrees (Smith et al., 2009; Chen et al., 2017; Liao et al., 2017a).

NOM-Mn(III) colloids formed at higher C/Mn ratio are less vulnerable to aggregation and thus have a higher degree of stability (Fig. 5). For both types of the HA, CCC values increased in both $CaCl_2$ and $MgCl_2$ solutions with increasing C/Mn ratio. For instance, the CCC value of AHA-Mn(III) colloids increased from 5.3 to 5.8 mM as the initial molar C/Mn ratio increased from 10 to 50 in $CaCl_2$ solutions, and 14.6 to 17 mM as the initial molar C/Mn ratio increased from 25 to 50 in $MgCl_2$ solutions (Fig. 5). Higher colloidal stability in the solutions with higher C/Mn ratios can be attributed to higher amounts of carboxylic groups from HA adsorbed on the colloidal surfaces, which contribute negative charge, thus relatively higher repulsion energy barriers between particles (Philippe and Schaumann, 2014). Supporting evidence of this phenomenon can be found in electrokinetic measurements (Fig. 6), which show that the zeta potential in both $CaCl_2$ and $MgCl_2$ solutions become more negative with an increase in molar C/Mn

ratio. Previous studies have also demonstrated that the ratio of NOM to metals plays a significant role in the stabilization of metal nanoparticles through electrostatic and/or steric interactions (Liao et al., 2017a,b). Note that the charge screening effect is more pronounced in the presence of Ca^{2+} compared to that of Mg^{2+} (Figs. S10), as also observed by others, due to the stronger complexation and bridging effect of Ca^{2+} relative to Mg^{2+} (Philippe and Schaumann, 2014), leading to higher aggregation potential, as indicated by the lower CCC values (Figs. 5c,f).

PPSHA-Mn(III) colloids are more stable against aggregation than AHA-Mn(III) colloids across the entire studied range of C/Mn ratios, as they show appreciably higher CCC values and lower aggregation rates for both $CaCl_2$ and $MgCl_2$ electrolytes (Figs. 5 and S11). Possible explanations of these observations can be related to the varied properties of HAs of different origins that may exert a dynamic influence on colloidal stability through multiple mechanisms including electrostatic interactions, hydration interactions, and steric hindrance (Philippe and Schaumann, 2014; Vindedahl et al., 2016). The HAs properties examined in our study included elemental composition, carbon functional group composition, and $SUVA_{254}$ (Table 2). As shown, higher $SUVA_{254}$ (an indicator of aromatic content) is a reflection of the higher aromatic content of AHA relative to PPSHA, which qualitatively agrees with the aromatic ratio determined by ^{13}C NMR (Table 2). However, the possibility of aromatic functionality exerting a stabilizing effect in particle aggregation can be largely ruled out as the CCC values of Ca^{2+} and Mg^{2+} for AHA-Mn(III) colloids were much lower than those for PPSHA-Mn(III) colloids (Fig. 5c,f). As previously discussed, PPSHA has more carboxylic groups than AHA (Fig. 2a, Table 2), thus relatively enhanced electrostatic repulsion (i.e. stability). This fact is

further supported by the higher negative charge of PPSHA-Mn(III) colloids compared to AHA-Mn(III) colloids (Fig. S12). Additionally, PPSHA is likely to be less hydrophobicity compared to AHA, as reflected by the lower aliphatic ratio (Table 2). Therefore, the higher stability of PPSHA-Mn(III) colloids may also be due to the relatively higher hydrophilicity of PPSHA, contributing to stronger repulsive hydration interactions (Xu et al., 2017). Further, steric hindrance originating from the adsorbed HA layer may also play an appreciable role in enhancing the stability of PPSHA-Mn(III), as observed by previous studies regarding the aggregation of metal- and carbon-based colloids (Huangfu et al., 2013; Aich et al., 2016; Liao et al., 2017a).

To provide additional insights into particle stability mechanisms of HA-Mn(III) colloids, we employed a theoretical model that integrates the zeta potential into the CCC expression based on classic DLVO theory, considering electrostatic repulsion and van der Waals attraction forces. Using the Derjaguin approximation, the relationship between CCC and surface potential of particles can be obtained by the following equations (see detailed derivation in the Supplementary Material) (Hsu and Kuo, 1997; Jiang et al., 2016):

$$CCC = nN_A \tag{3}$$

$$n = \frac{\lambda \tanh^4\left(\frac{a\psi_0}{4}\right)}{a^5(a+b)k_3^6} \frac{(4\pi\varepsilon_0\varepsilon_r)^3(k_BT)^5 48^2}{e^6 {A_{131}}^2 \pi \exp(2)} \tag{4}$$

$$\lambda = \left[1 - \frac{1}{2k_3X_0}\left(1 - \exp(-2k_3X_0)\right)\right]^2 \tag{5}$$

where n is the number concentration of cations in bulk phase, λ is a parameter calculated to be 1.0 for all the scenarios in this study, N_A is the Avogadro's number (6.02×10^{23} mol^{-1}), ψ_0 is the dimensionless surface potential (V), a and b are the valences of

cation and anion of the electrolyte respectively, ε_0 is the dialectic permittivity in vacuum (8.854×10^{-12} C^2/J/m), ε_r is the relative dialectic permeability of water (78.5), k_B is the Boltzmann's constant (1.38×10^{-23} J/K), T is the absolute temperature (298 K), k_3 is a parameter related to a and b (for $CaCl_2$ and $MgCl_2$, $k_3 \approx 1.078$), e is the elementary charge of an electron (1.60×10^{-19} C), A_{131} is the Hamaker constant of HA-Mn(III) colloids in water (J), and X_0 is the dimensionless radius of the particle (m).

Equations 3-5 show that CCC is proportional to zeta potential. We plotted CCC with $\tanh^4\left(\frac{a\psi_0}{4}\right)$ and found that they display a strong linear correlation ($R^2 > 0.97$) regardless of the electrolytes (Fig. 7a-d). This reinforces a strong dominance of DLVO-type interactions in governing HA-Mn(III) colloids stability. However, we note that the extrapolation of the fitting lines does not across zero, implying that the additional non-DLVO interactions such as hydration interactions and steric hindrance described above may also have contributed to the enhanced stability of HA-Mn(III) colloids. Further, the higher slope observed in PPSHA systems also likely supports higher observed CCC values of PPSHA-Mn(III) colloids relative to AHA-Mn(III) colloids.

The Hamaker constant of HA-Mn(III) colloids in water estimated from eq 4 can range from $1.72\text{-}4.06 \times 10^{-20}$ J. This is within the same order of magnitude, but is lower than the Hamaker constant for MnO_2 colloids in aqueous solution (7.84×10^{-20} J, Huangfu et al., 2013). The derived Hamaker constant can be then used to calculate the DLVO interaction energies. DLVO profiles clearly show that an increase in C/Mn ratios increased the repulsion energy barrier potential, resulting in higher electrostatic and electrosteric repulsion (Fig. 7e,f). The repulsion energy barrier was higher for PPSHA-Mn(III)

colloids than that for AHA-Mn(III) colloids (Fig. 7e,f), indicating relatively higher aggregation resistance for PPSHA-Mn(III) colloids.

3.4. Stability of NOM-Mn(III) colloids in natural aqueous matrices

The colloidal stability mechanisms explored above in simple solutions can be used to assess the stability of HA-Mn(III) colloids in more complex natural waters (Fig. 8). In a river water sample, the equivalent ionic strength of cations is considerably lower than the estimated CCC values for divalent electrolytes (i.e., Ca^{2+} and Mg^{2+}) (Table S1). Consequently, a near complete stabilization of NOM-Mn(III) colloids was observed as the particle's hydrodynamic diameter remained unchanged (1 h) (Fig. 8a,b). In groundwater, by contrast, the ionic strength is much higher than the CCC values (Table S1), a rapid aggregation of HA-Mn(III) colloids was observed with a particle size increase from starting ~ 200 nm quickly to > 1000 nm within the first 30 min (Fig. 8a,b). Such a disparity in HA-Mn(III) colloids stabilization suggest that the CCC value may be an indicator of overall colloidal stability in natural waters, consistent with the similar findings from other studies (Smith et al., 2009; Chen et al., 2017). Although the groundwater also contained high concentrations of Na^{+}, Cl^{-}, and SO_4^{2-} (Table S1), the influence of these ions on the stability of HA-Mn(III) colloids was minimal due to the insignificant change of hydrodynamic diameter in controlled experiments (not shown). When the groundwater was diluted with DI water, aggregation rate was monotonically decreased as the groundwater proportion decreased (Fig. 8c), owing to the decrease in the fractions of Ca^{2+} and Mg^{2+}. At the groundwater-to-DI ratio of 1:4, no appreciably aggregation was observed due to the much lower divalent electrolytes compared to the

509 CCC value for Ca^{2+} and Mg^{2+}. Consistent with the CCC values, the aggregation rate of
510 PPSHA-Mn(III) colloids was lower than that of AHA-Mn(III) colloids (Fig. 8c).
511

512 ## 4. Conclusions

513 This is the first report on the formation and stability of NOM-Mn(III) colloids in
514 aqueous systems. Based on a suite of complementary characterization techniques, it can
515 be concluded that relative amount and stability of HA-Mn(III) colloids generally
516 increases with increasing molar C/Mn ratios, and that HA with more surface
517 deprotonated COO^- group and hydrophilicity result in higher stability likely due to
518 (stronger) electrostatic repulsion, hydration interactions, and steric hindrance. This study
519 also supports the use of CCC values (focused on divalent cations) as a relatively simple
520 index to evaluate colloidal stability in natural water samples. Overall, the results provide
521 valuable insights towards understanding of C and Mn geochemistry in aqueous systems,
522 which also have implications regarding the fate and transport of associated contaminants,
523 nutrients, and trace metals. As observed, the stability of HA-Mn(III) colloids in fluvial
524 systems likely enhances the transport of Mn and C to the coast, influencing the deposition
525 and mass flux, and the fractionation of Mn and C along the salinity gradients in estuary
526 systems. HA-Mn(III) colloids with enhanced stability at higher C/Mn ratios may exert a
527 profound influence on the transport and transformation of contaminants as Mn(III) is
528 highly redox active and can donate and/or accept electrons. We recognize that natural
529 environments are more complicated than systems presented, further studies are therefore
530 needed to investigate such redox properties and long-term stability of NOM-Mn(III)
531 colloids in realistic aquatic systems.

Acknowledgments

This work was supported by the Natural Science Foundation of China (No. 41703128, 41572228, 41521001), the Basic Research Project of Shenzhen (JCYJ20170307110055182), the China Postdoctoral Science Foundation (2017M610530), the Southern University of Science and Technology (SUSTC) (G01296001), and the Program for Guangdong Introducing Innovative and Entrepreneurial Teams (2017ZT07Z479). The authors are also grateful to the Pico Center at SUSTC, supported by the Presidential Fund and Development and Reform Commission of Shenzhen Municipality.

Appendix A. Supplementary data

Additional information includes experimental and theoretical descriptions (sections S1–S2), Figs. S1–S12, and Tables S1–S3.

References

Aich, N., Boateng, L.K., Sabaraya, I.V., Das, D., Flora, J.R.V., Saleh, N.B., 2016. Aggregation kinetics of higher-order fullerene clusters in aquatic systems. Environ. Sci. Technol. 50, 3562−3571.

Chen, C., Dynes, J., Wang, J., Sparks, D.L., 2014. Properties of Fe-organic matter associations via coprecipitation versus adsorption. Environ. Sci. Technol. 48, 13751−13759.

Chen, C., Huang, W., 2017. Aggregation kinetics of diesel soot nanoparticles in wet environments. Environ. Sci. Technol. 51, 2077−2086.

Chen, K.L., Mylon, S., Elimelech, M., 2006. Aggregation kinetics of alginate-coated hematite nanoparticles in monovalent and divalent electrolytes. Environ. Sci. Technol. 40, 1516−1523.

Elimelech, M., Gregory, J., Jia, X., Williams, R.A., 1995. *Particle deposition and aggregation: measurement, modeling, and simulation*. Butterworth-Heinemann: Oxford, England.

Fanun, M., 2014. *The role of colloidal systems in environmental protection*. Elsevier, Oxford, UK.

560 Gao, Y., Jiang, J., Zhou, Y., Pang, S., Jiang, C., Guo, Q., Duan, J., 2018. Does soluble Mn(III)
561 oxidant formed in situ account for enhanced transformation of triclosan by Mn(VII) in the
562 presence of ligands? Environ. Sci. Technol. 52, 4785−4793.
563 Gude, J.C.J., Rietveld, L.C., van Halem, D., 2017. As(III) oxidation by MnO_2 during groundwater
564 treatment. Water Res. 111, 41−51.
565 Hsu, J.P., Kuo, Y.C., 1997. The critical coagulation concentration of counterions: spherical particles
566 in asymmetric electrolyte solutions. J. Colloid Interface Sci. 185, 530−537.
567 Hu, E., Zhang, Y., Wu, S., Wu, J., Liang, L., He, F., 2017. Role of dissolved Mn(III) in
568 transformation of organic contaminants: Non-oxidative versus oxidative mechanisms. Water Res.
569 111, 234−243.
570 Huangfu, X., Jiang, J., Ma, J., Liu, Y., Yang, J., 2013. Aggregation kinetics of manganese dioxide
571 colloids in aqueous solution: influence of humic substances and biomacromolecules. Environ. Sci.
572 Technol. 47, 10285−10292.
573 Jiang, Y., Raliya, R., Fortner, J.D., Biswas, P., 2016. Graphene oxides in water: correlating
574 morphology and surface chemistry with aggregation behavior. Environ. Sci. Technol. 50,
575 6964−6973.
576 Jiang, Y., Raliya, R., Liao, P., Biswas, P., Fortner, J.D., 2017. Graphene oxides in water: assessing
577 stability as a function of material and natural organic matter propterties. Environ. Sci.: Nano 4,
578 1484−1493.
579 Johnson, K.S., 2006. Manganese redox chemistry revisited. Science 313, 1896−1897.
580 Julien, C.M., Massot, M., Poinsignon, C., 2004. Lattice vibrations of manganese oxides Part I.
581 periodic structures. Spectrochim. Acta Part A 60, 689−700.
582 Li, W., Liu, D., Wu, J., Kim, C., Fortner, J.D., 2014. Aqueous aggregation and surface deposition
583 processes of engineered superparamagnetic iron oxide nanoparticles for environmental
584 applications. Environ. Sci. Technol. 48, 11892−11900.
585 Liao, P., Li, W., Jiang, Y., Wu, J., Yuan, S.H, Fortner J.D., Giammar, D.E., 2017a. Formation,
586 aggregation, and deposition dynamics of NOM-Iron colloids at anoxic-oxic interfaces. Environ.
587 Sci. Technol. 51 (21), 12235−12245.
588 Liao, P., Li, W.L., Wang, D.G., Jiang, Y., Pan, C., Fortner, J.D., Yuan, S. H., 2017b. Effect of
589 reduced humic acid on the transport of ferrihydrite nanoparticles under anoxic conditions. Water
590 Res. 109, 347−357.
591 Luther III, G.W., 2005. Manganese (II) oxidation and Mn (IV) reduction in the environment-two
592 one-electron transfer steps versus a single two-electron step. Geomicrobiol. J. 22, 195−203.
593 Madison, A.S., Tebo, B.M., Luther, G.W., 2011. Simultaneous determination of soluble
594 manganese(III), manganese(II) and total manganese in natural (pore)waters. Talanta 84, 374−381.
595 Madison, A.S., Tebo, B.M., Mucci, A., Sundby, B., Luther, G.W., 2013. Abundant porewater Mn(III)
596 is a major component of the sedimentary redox system. Science 341, 875−878.
597 Mao, J.D., Hu, W.G., Schmidt-Rohr, K., Davies, G., Ghabbour, E.A., Xing, B.S., 2000. Quantitative
598 characterization of humic substances by solid-state carbon-13 nuclear magnetic resonance. Soil
599 Sci. Soc. Am. J. 64, 873–884.
600 Mensch, A.C., Hernandez, R.T., Kuether, J.E., Torelli, M.D., Feng, Z.V., Hamers, R.J., Pedersen,
601 J.A., 2017. Natural organic matter concentration impacts the interaction of functionalized
602 diamond nanoparticles with model and actual bacterial membranes. Environ. Sci. Technol. 51,
603 11075−11084.

Meyer, W., Kons, S., Achten, C., 2015. Impact of reference geosorbents on oral bioaccessibility of PAH in a human in vitro digestive tract model. Environ. Sci. Pollut. Res. 22, 5164–5170.
Myneni, S.C.B., Brown, J.T., Martinez, G.A., Meyer-Ilse, W., 1999. Imaging of humic substance macromolecular structures in water and soils. Science 286, 1335–1337.
Oldham, V.E., Mucci, A., Tebo, B.M., Luther, G.W., 2017a. Soluble Mn(III)-L complexes are abundant in oxygenated waters and stabilized by humic ligands. Geochim. Cosmochim. Acta 199, 238–246.
Oldham, V.E., Miller M.T., Jensen L.T., Luther, G.W., 2017b. Revisiting Mn and Fe removal in humic rich estuaries. Geochim. Cosmochim. Acta 209, 267–283.
Oldham, V.E., 2017. *The complexation chemistry of dissolved manganese(III) in the ocean and its role in the coupled cycles of carbon, iron, and sulfur*. PhD thesis, University of Delaware.
Oleinikova, O.V., Shirokova, L.S., Gérard, E., Drozdova, O.Y., Lapitskiy, S.A., Bychkov, A.Y., Pokrovsky, O.S., 2017. Transformation of organo-ferric peat colloids by a heterotrophic bacterium. Geochim. Cosmochim. Acta 205, 313–330.
Pennycook, S.J., Nellist, P.D., 2011. *Scanning transmission electron microscopy: imaging and analysis*. Springer.
Philippe, A., Schaumann, G.E., 2014. Interactions of dissolved organic matter with natural and engineered inorganic colloids: A review. Environ. Sci. Technol. 48, 8946–8962.
Pokrovsky, O.S., Schott, J., 2002. Iron colloids/organic matter associated transport of major and trace elements in small boreal rivers and their estuaries (NW Russia). Chem. Geol. 190, 141–179.
Post, J.E., 1999. Manganese oxide minerals: Crystal structures and economic and environmental significance. Proc. Natl. Acad. Sci. USA. 96, 3447–3454.
Saleh, N.B., Pfefferle, L.D., Elimelech, M., 2008. Aggregation kinetics of multiwalled carbon nanotubes in aquatic systems: measurements and environmental implications. Environ. Sci. Technol. 42, 7963-7969.
Sharma, P., Ofner, J., Kappler, A., 2010. Formation of binary and ternary colloids and dissolved complexes of organic matter, Fe and As. Environ. Sci. Technol. 44, 4479–4485.
Smith, B., Wepasnick, K., Schrote, K.E., Bertele, A.R., Ball, W.P., O'Melia, C., Fairbrother, D.H., 2009. Colloidal properties of aqueous suspensions of acid-treated, multi-walled carbon nanotubes. Environ. Sci. Technol. 43, 819–825.
Stumm, W., Morgan, J.J., 1996. *Aquatic Chemistry*. Wiley-Interscience, New York.
Sun, B., Guan, X., Fang, J., Tratnyek, P.G., 2015. Activation of manganese oxidants with bisulfite for enhanced oxidation of organic contaminants: the involvement of Mn(III). Environ. Sci. Technol. 49, 12414–12421.
Sunda, W.G., Kieber, D.J., 1994. Oxidation of humic substances by manganese oxides yields low molecular-weight organic substrates. Nature 367, 62–64.
Trouwborst, R.E., Clement, B.G., Tebo, B.M., Glazer, B.T., Luther, G.W., 2006. Soluble Mn(III) in suboxic zones. Science 313, 1955–1957.
Vindedahl, A.M., Strehlau, J.H., Arnold, W.A., Penn, R.L., 2016. Organic matter and iron oxide nanoparticles: aggregation, interactions, and reactivity. Environ. Sci.: Nano 3, 494–505.
Wu, J.F., Boyle, E., Sunda, W., Wen, L.S., 2001. Soluble and colloidal iron in the oligotrophic North Atlantic and North Pacific. Science 293, 847–849.

Xu, F., Wei, C., Zeng, Q., Li, X., Alvarez, P.J.J., Li, Q., Qu, X., Zhu, D., 2017. Aggregation behavior of dissolved black carbon: implications for vertical mass flux and fractionation in aquatic systems. Environ. Sci. Technol. 51, 13723−13732.

Yakushev, E.V., 2013. *Chemical structure of pelagic redox interfaces: observation and modeling*. Hdb Env Chem 22: 67-94. DOI 10.1007/698_2010_84, Springer-Verlag Berlin Heidelberg.

Zhang, J., Ma J., Song, H., Sun, S., Zhang, Z., Yang, T., 2018. Organic contaminants degradation from the S(IV) autoxidation process catalyzed by ferrous-manganous ions: A noticeable Mn(III) oxidation process. Water Res. 133, 227−235.

Table 1 Summary of the experiments performed

Content	Conditions	Objective
1-Colloid formation	Varied molar C/Mn ratios (0-50); different HA types (AHA and PPSHA)	Decipher the role of C/Mn ratios and HA types on HA-Mn(III) colloids formation
2-Colloid characterization	FTIR, XPS, DLS, zeta potential, XRD, UV-vis, and ultrahigh resolution Cs-STEM-EDS	Identify the surface properties, morphology, and structure of formed HA-Mn(III) colloids
3-Colloid stability mechanisms	Varied $CaCl_2$: 0-40 mM Varied $MgCl_2$: 0-100 mM	Determine early-stage aggregation kinetics, critical coagulation concentrations, and stability mechanisms
4-Colloid stability in natural waters	Surface river water Groundwater	Evaluate the colloidal stability in more complex natural waters to develop a predictive model

Table 2 HA characteristics [a]

Sample	Bulk elemental composition (%)					Functional group composition				$SUVA_{254}$
	C	H	O	N	S	Carboxylic	Aromatic	Carbohydrate	Aliphatic	L/mg/m
AHA	47.3	3.1	44.9	1.2	3.5	15.6 ± 2.2	45.1 ± 6.3	6.0 ± 0.5	33.4± 3.0	9.5 ± 0.4
PPSHA	46.9	3.9	30.3	3.42	0.58	21.4	40.3	21.4	16.9	8.7 ± 0.3

[a]Bulk elemental compositions for AHA were determined by Vario Micro cube elemental analyzer. Bulk elemental compositions for PPSHA were provided by International Humic Substances Society (IHSS, http://humic-substances.org/). Functional group composition for both HAs were determined by ^{13}C nuclear magnetic resonance (NMR), as reported by Mao et al. (2000).

Table 1 Summary of the experiments performed

Content	Conditions	Objective
1-Colloid formation	Varied molar C/Mn ratios (0-50); different HA types (AHA and PPSHA)	Decipher the role of C/Mn ratios and HA types on HA-Mn(III) colloids formation
2-Colloid characterization	FTIR, XPS, DLS, zeta potential, XRD, UV-vis, and ultrahigh resolution Cs-STEM-EDS	Identify the surface properties, morphology, and structure of formed HA-Mn(III) colloids
3-Colloid stability mechanisms	Varied $CaCl_2$: 0-40 mM Varied $MgCl_2$: 0-100 mM	Determine early-stage aggregation kinetics, critical coagulation concentrations, and stability mechanisms
4-Colloid stability in natural waters	Surface river water Groundwater	Evaluate the colloidal stability in more complex natural waters to develop a predictive model

Table 2 HA characteristics [a]

Sample	Bulk elemental composition (%)					Functional group composition				$SUVA_{254}$
	C	H	O	N	S	Carboxylic	Aromatic	Carbohydrate	Aliphatic	L/mg/m
AHA	47.3	3.1	44.9	1.2	3.5	15.6 ± 2.2	45.1 ± 6.3	6.0 ± 0.5	33.4± 3.0	9.5 ± 0.4
PPSHA	46.9	3.9	30.3	3.42	0.58	21.4	40.3	21.4	16.9	8.7 ± 0.3

[a]Bulk elemental compositions for AHA were determined by Vario Micro cube elemental analyzer. Bulk elemental compositions for PPSHA were provided by International Humic Substances Society (IHSS, http://humic-substances.org/). Functional group composition for both HAs were determined by ^{13}C nuclear magnetic resonance (NMR), as reported by Mao et al. (2000).

Figures

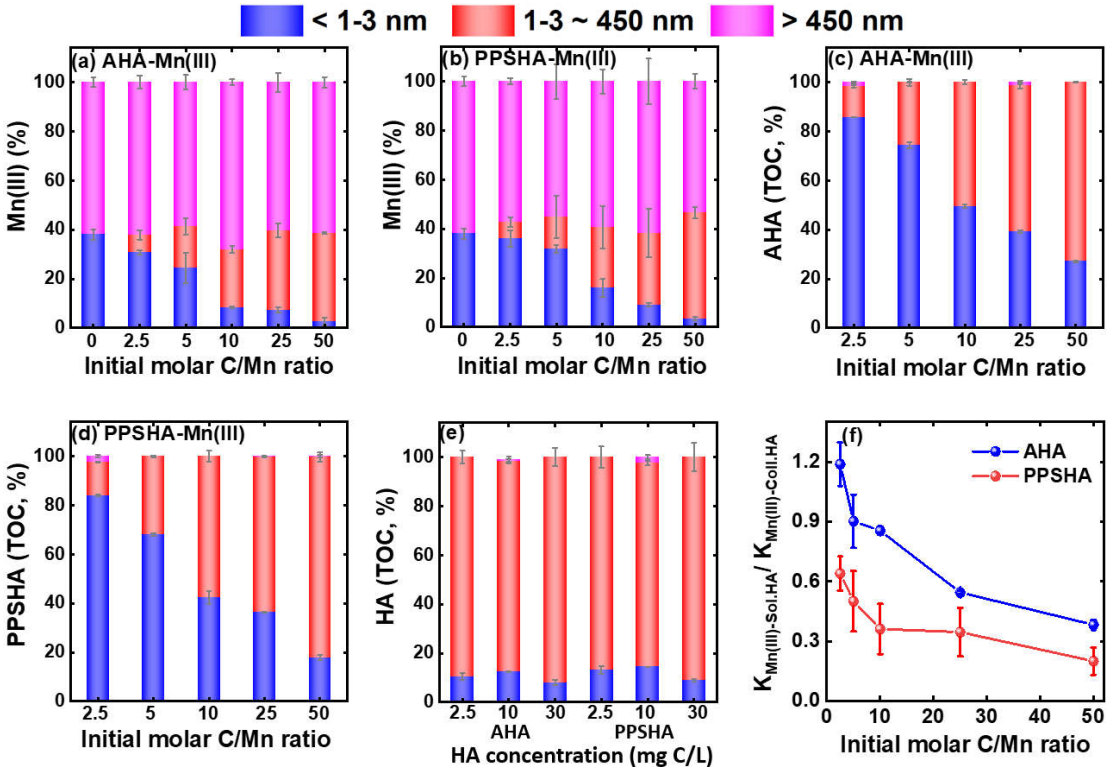

Fig. 1 Formation of HA-Mn(III) colloids. Percentage of (a,b) Mn and (c,d) HA concentrations in (a,c) AHA-Mn(III) suspension and (b,d) PPSHA-Mn(III) suspension in different size fractions at steady-state conditions as a function of initial C/Mn molar ratios. (e) Percentage of HA concentrations in (a,c) AHA-Mn(III) suspension and (b,d) PPSHA-Mn(III) suspension in the size fractions as a function of initial HA concentration (control experiments without Mn(III)). The percentage in y-axis means the concentration of (a,b) Mn(III) and (c-e) HA in a certain size fraction to the total concentration of Mn and HA in the suspension. Please note that all Mn in our study was Mn(III). (f) The evaluated $K_{Mn(III)\text{-}Sol.HA}/ K_{Mn(III)\text{-}Coll.HA}$ as a function of initial C/Mn molar ratios. $K_{Mn(III)\text{-}Sol.HA}/ K_{Mn(III)\text{-}Coll.HA}$ = ([Sol. Mn(III)]/[Coll. Mn(III)])×([Coll. HA]/[Sol. HA]), where [Sol. Mn(III)] and [Coll. Mn(III)] are the truly soluble and colloidal Mn(III) concentration, respectively, [Sol. HA] and [Coll. HA] are the truly soluble and colloidal HA concentration, respectively. Error bars represent standard deviations of at least duplicate measurements.

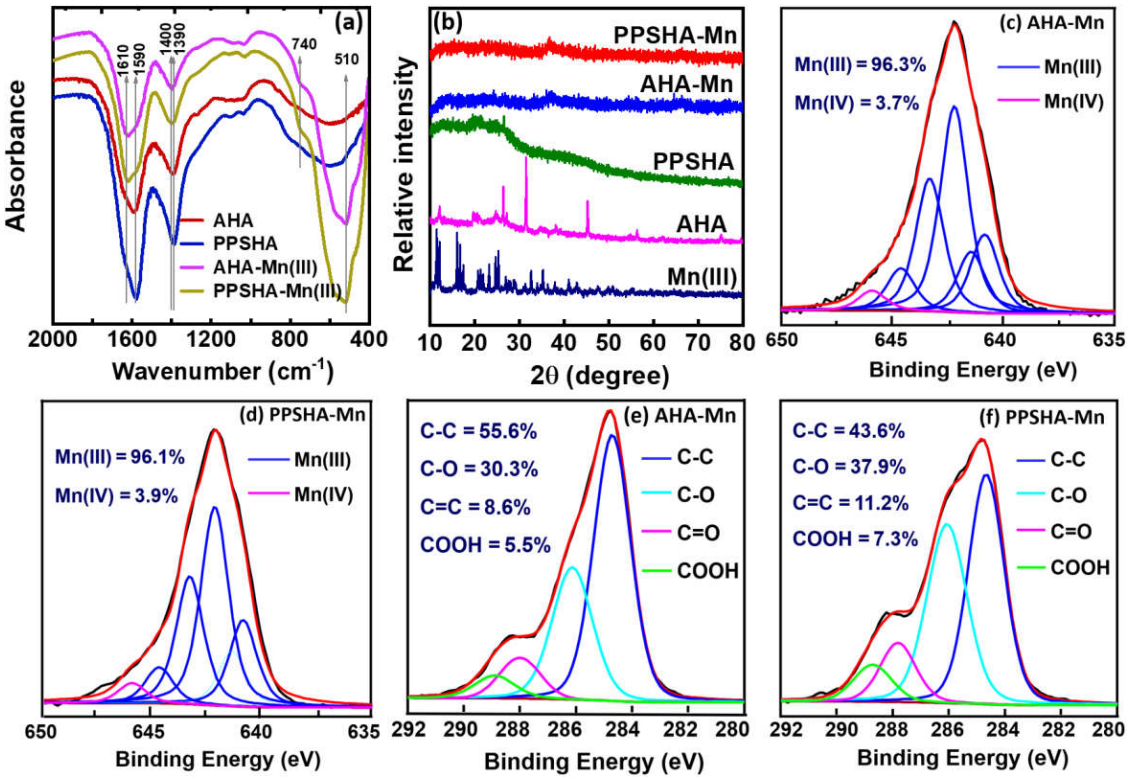

Fig. 2 Properties of HA-Mn(III) colloids. (a) FTIR spectra of HA-Mn(III) colloids and HAs alone (no Mn(III) added). (b) XRD patterns of HA-Mn(III) colloids. For reference, the patterns of pure HAs and Mn(III) (as Mn(III) acetate dihydrate) are included in XRD plots. The values of 2θ are those for copper Ka X-rays. (c-f) high resolution (c,d) Mn $2p_{3/2}$ XPS spectra and (e,f) C1s XPS spectra of HA-Mn(III) colloids. FTIR, XRD, and XPS analysis of solid samples were obtained at a fixed initial molar C/Mn ratio of 50. The binding energies of surface Mn species for fitting the Mn $2p_{3/2}$ peak of the solid product and the relative area of each multiplet for the surface species were provided in Table S3.

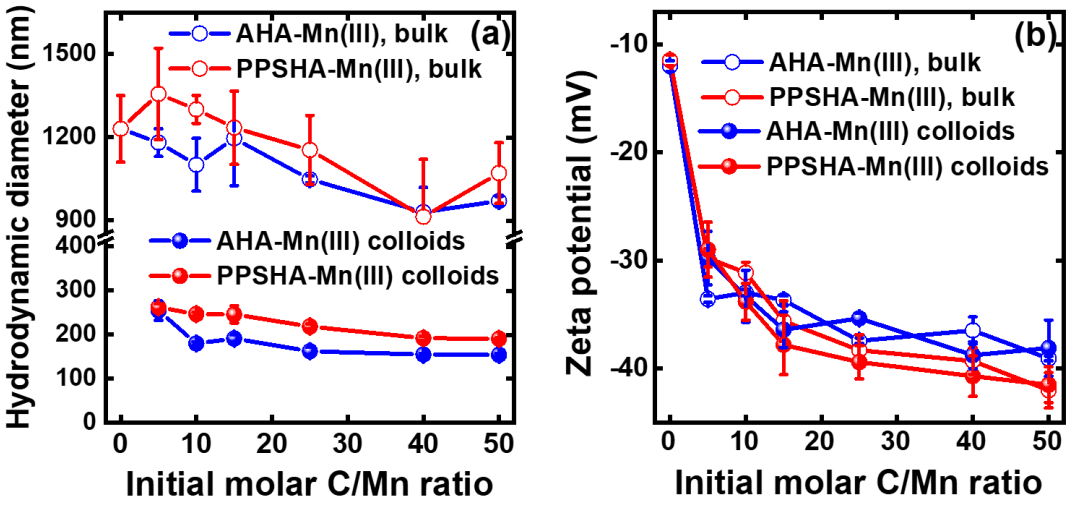

Fig. 3 (a) Z-averaged hydrodynamic diameter and (b) zeta potential of HA-Mn(III) colloids (1-3 to 450 nm) and larger particles in HA-Mn(III) suspensions (without any filtration treatments) at steady-state conditions as a function of initial C/Mn molar ratios. Each data refers to the mean of 10 measurements of duplicate samples. Error bars represent standard deviations.

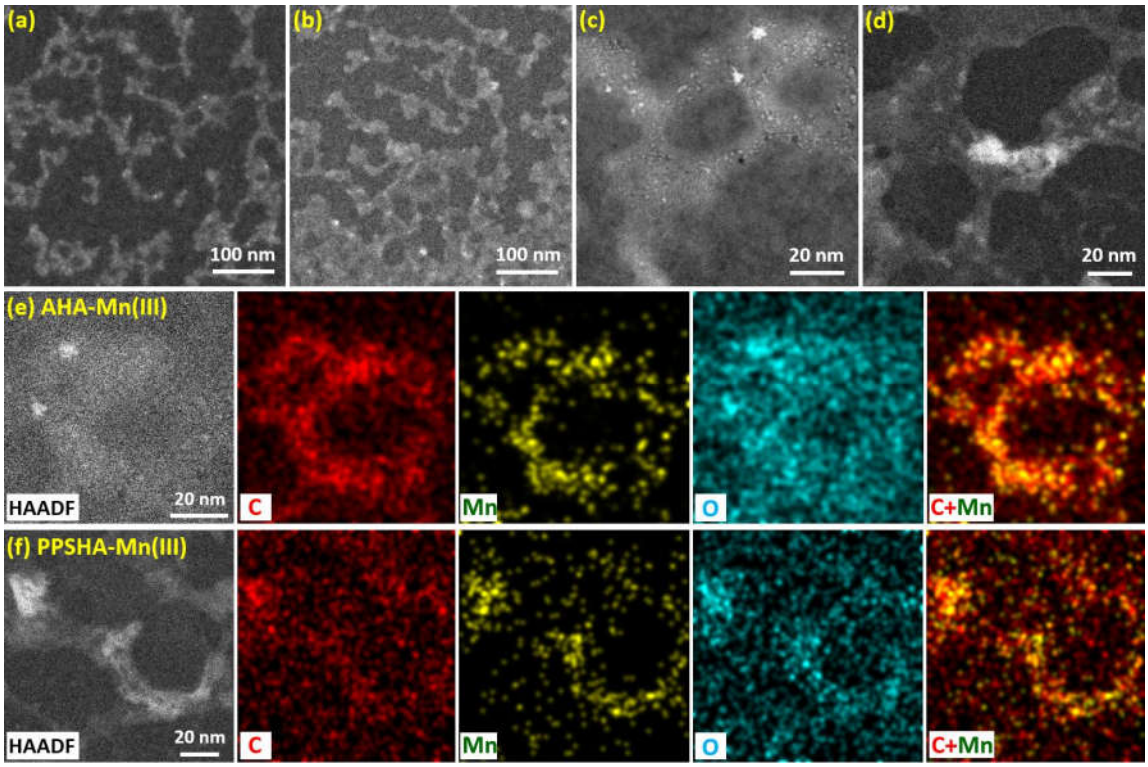

Fig. 4 Morphology and microscopic structure of HA-Mn(III) colloids. STEM images of (a,c) AHA-Mn(III) colloids and (b,d) PPSHA-Mn(III) colloids. HAADF images of (e) AHA-Mn(III) colloids and (f) PPSHA-Mn(III) colloids and the corresponding high-resolution EDS elemental mappings of C, Mn, and O, and color overlays of C and Mn. Both AHA-Mn(III) and PPSHA-Mn(III) colloids were imaged at an initial molar C/Mn ratio of 50.

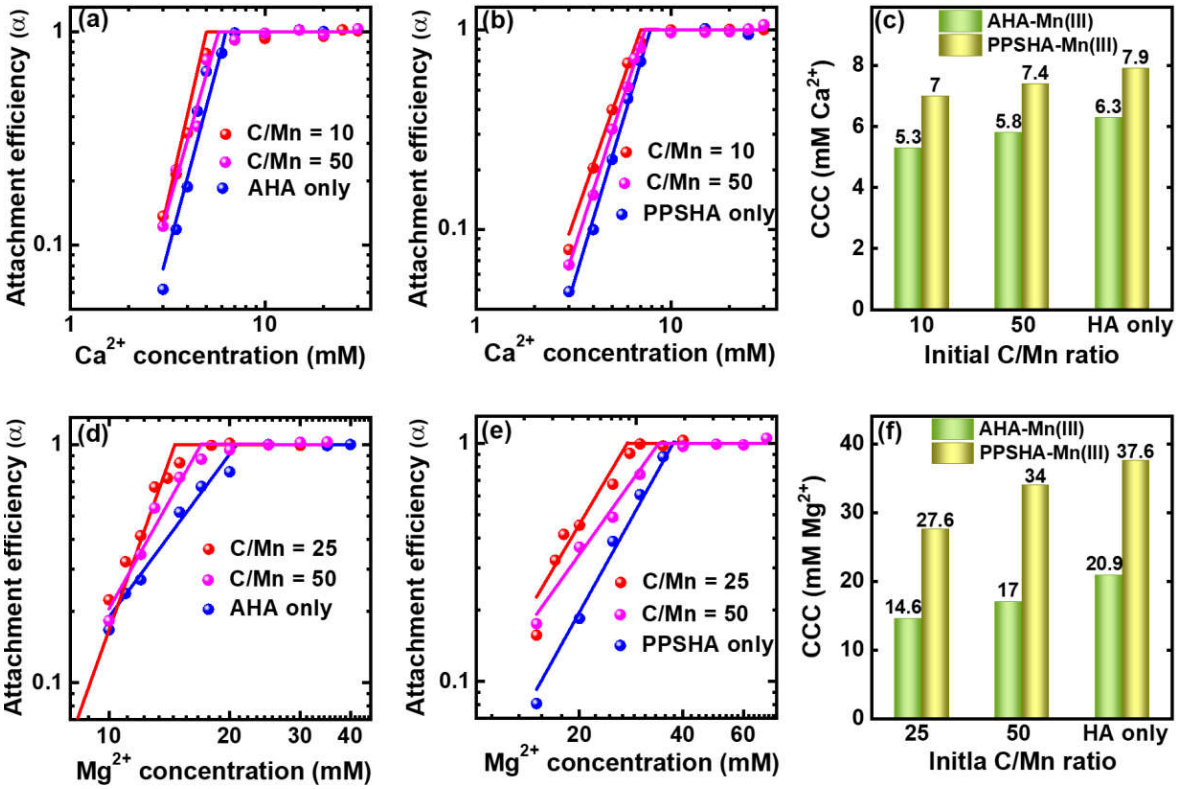

Fig. 5 Attachment efficiency of (a,d) AHA-Mn(III) colloids and (b,e) PPSHA-Mn(III) colloids for different C/Mn molar ratios as a function of concentrations of (a, b) Ca^{2+} and (d, e) Mg^{2+} at pH 7. The corresponding critical coagulation concentration (CCC), which was summarized in panels c and f, was derived by intersection of extrapolations through reaction-limited and diffusion-limited regimes as an index of particle aqueous stability.

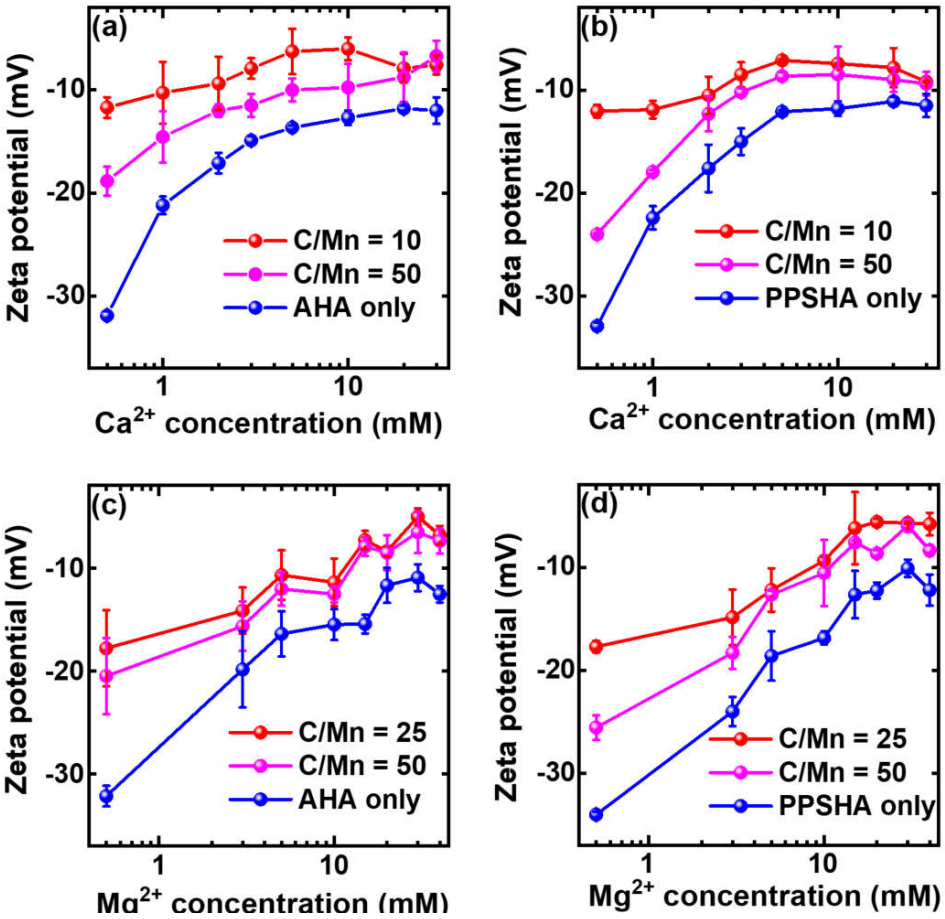

Fig. 6 Zeta potentials of different C/Mn molar ratios of (a,c) AHA-Mn(III) colloids and (b,d) PPSHA-Mn(III) colloids respectively over a range of (a, b) Ca^{2+} and (c, d) Mg^{2+} concentrations at pH 7. Each data point shows the mean of 10 measurements of duplicate samples. Error bars represent standard deviations.

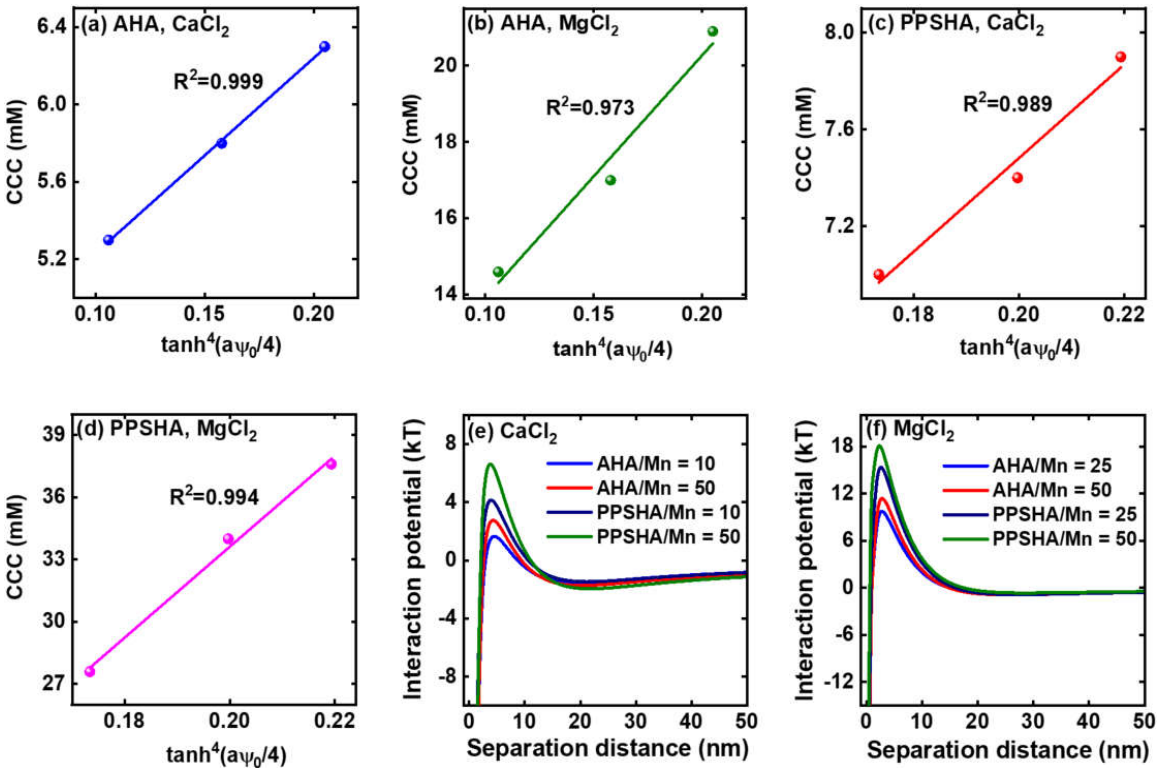

Fig. 7 (a-d) Correlation between the CCC values of HA-Mn(III) colloids and the zeta potentials. (e,f) Estimated total interaction energy as a function of separation distance using DLVO theory for HA-Mn(III) colloids at different initial molar C/Mn ratios in the presence of 1 mM (e) $CaCl_2$ and (f) $MgCl_2$.

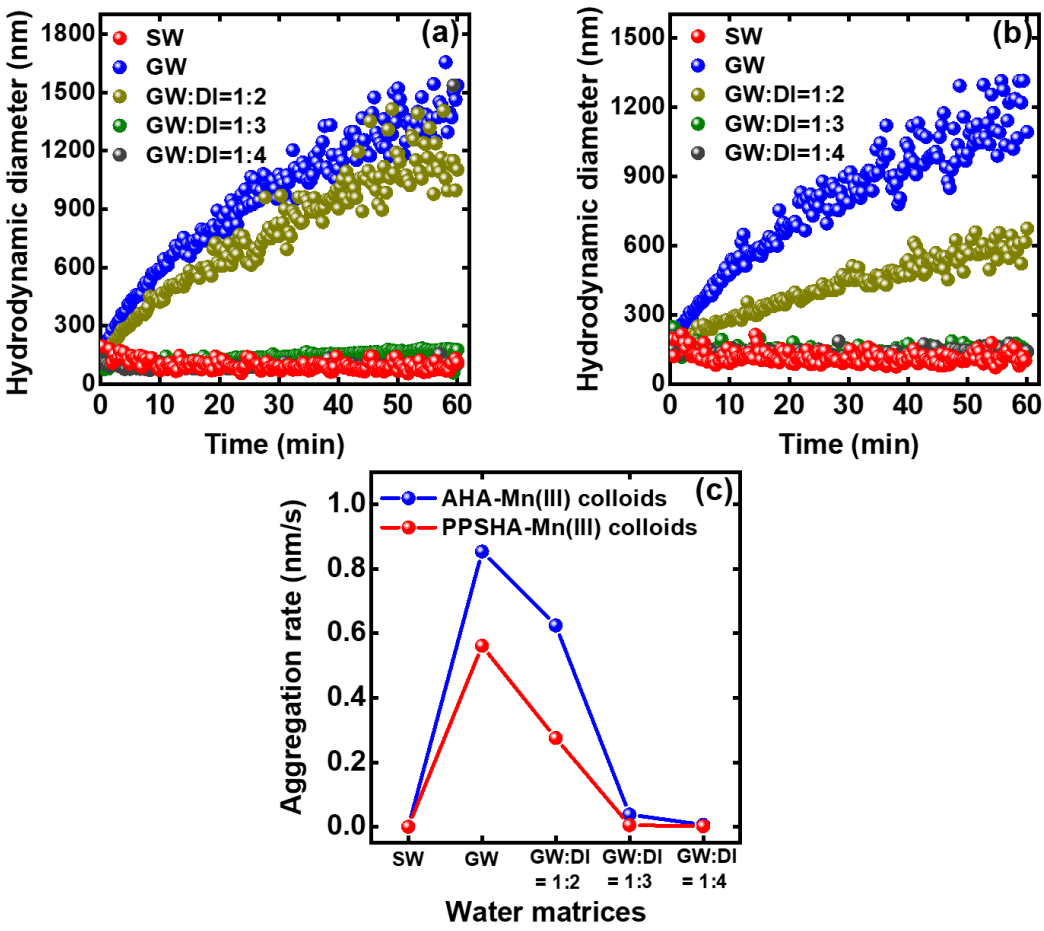

Fig. 8 The aggregation profiles of (a) AHA-Mn(III) colloids and (b) PPSHA-Mn(III) colloids, and (c) the corresponding initial aggregation rate in surface river water, groundwater, and groundwater with DI water for different mixtures. No appreciable aggregation was observed in the absence of HA-Mn(III) colloids, demonstrating that aggregation is due to the introduction of HA-Mn(III) colloids other than other impurities in waters. Aggregation rates were quantified from the initially linear increase in hydrodynamic diameter over time as described in section 2.3.

Figures Marked

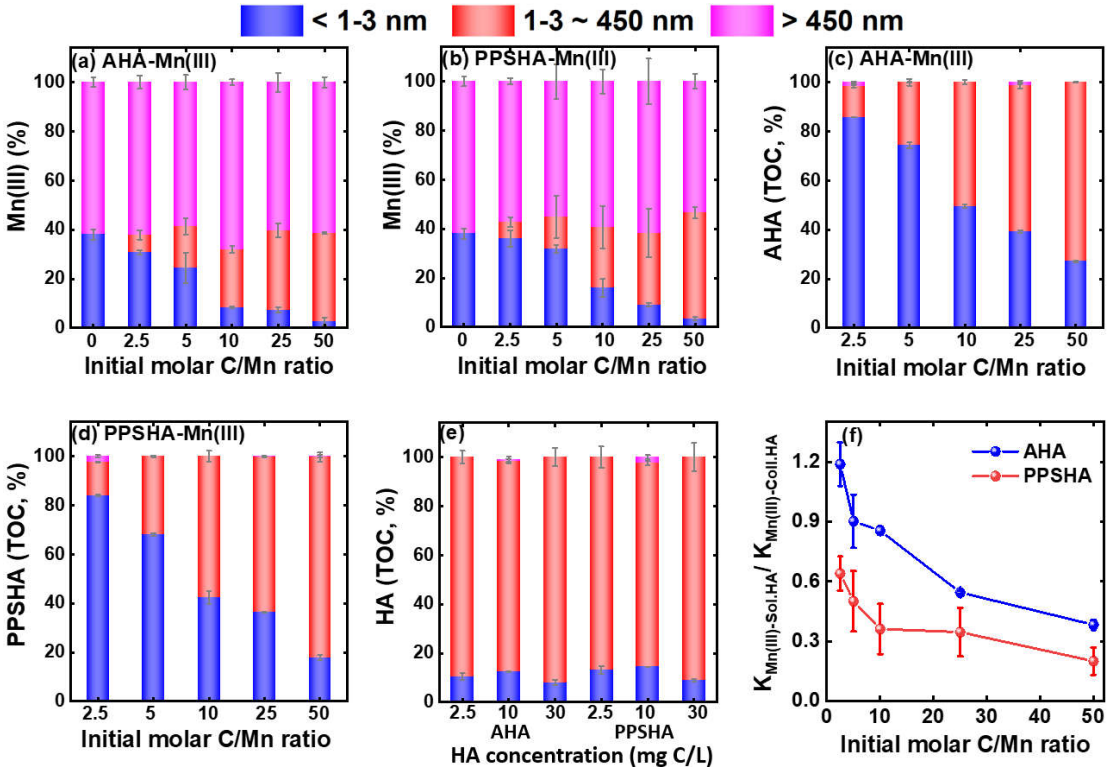

Fig. 1 Formation of HA-Mn(III) colloids. Percentage of (a,b) Mn and (c,d) HA concentrations in (a,c) AHA-Mn(III) suspension and (b,d) PPSHA-Mn(III) suspension in different size fractions at steady-state conditions as a function of initial C/Mn molar ratios. (e) Percentage of HA concentrations in (a,c) AHA-Mn(III) suspension and (b,d) PPSHA-Mn(III) suspension in the size fractions as a function of initial HA concentration (control experiments without Mn(III)). The percentage in y-axis means the concentration of (a,b) Mn(III) and (c-e) HA in a certain size fraction to the total concentration of Mn and HA in the suspension. Please note that all Mn in our study was Mn(III). (f) The evaluated $K_{Mn(III)\text{-}Sol.HA}$/ $K_{Mn(III)\text{-}Coll.HA}$ as a function of initial C/Mn molar ratios. $K_{Mn(III)\text{-}Sol.HA}$/ $K_{Mn(III)\text{-}Coll.HA}$ = ([Sol. Mn(III)]/[Coll. Mn(III)])×([Coll. HA]/[Sol. HA]), where [Sol. Mn(III)] and [Coll. Mn(III)] are the truly soluble and colloidal Mn(III) concentration, respectively, [Sol. HA] and [Coll. HA] are the truly soluble and colloidal HA concentration, respectively. Error bars represent standard deviations of at least duplicate measurements.

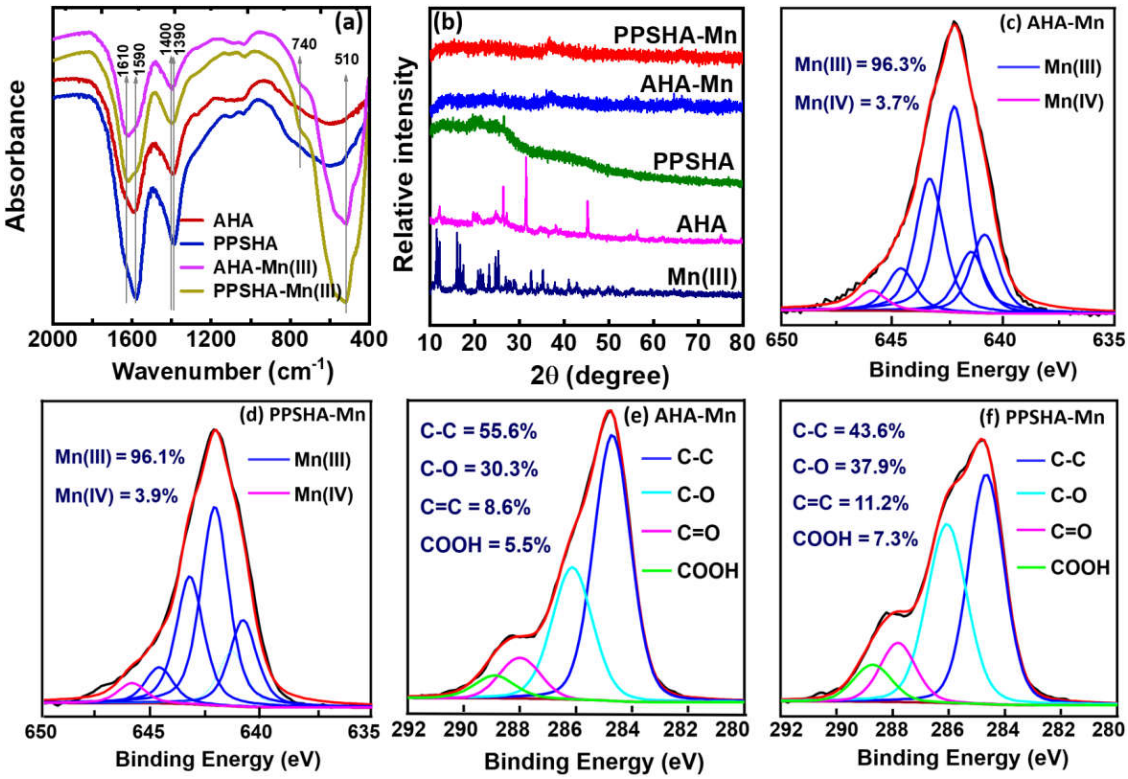

Fig. 2 Properties of HA-Mn(III) colloids. (a) FTIR spectra of HA-Mn(III) colloids and HAs alone (no Mn(III) added). (b) XRD patterns of HA-Mn(III) colloids. For reference, the patterns of pure HAs and Mn(III) (as Mn(III) acetate dihydrate) are included in XRD plots. The values of 2θ are those for copper Ka X-rays. (c-f) high resolution (c,d) Mn $2p_{3/2}$ XPS spectra and (e,f) C1s XPS spectra of HA-Mn(III) colloids. FTIR, XRD, and XPS analysis of solid samples were obtained at a fixed initial molar C/Mn ratio of 50. The binding energies of surface Mn species for fitting the Mn $2p_{3/2}$ peak of the solid product and the relative area of each multiplet for the surface species were provided in Table S3.

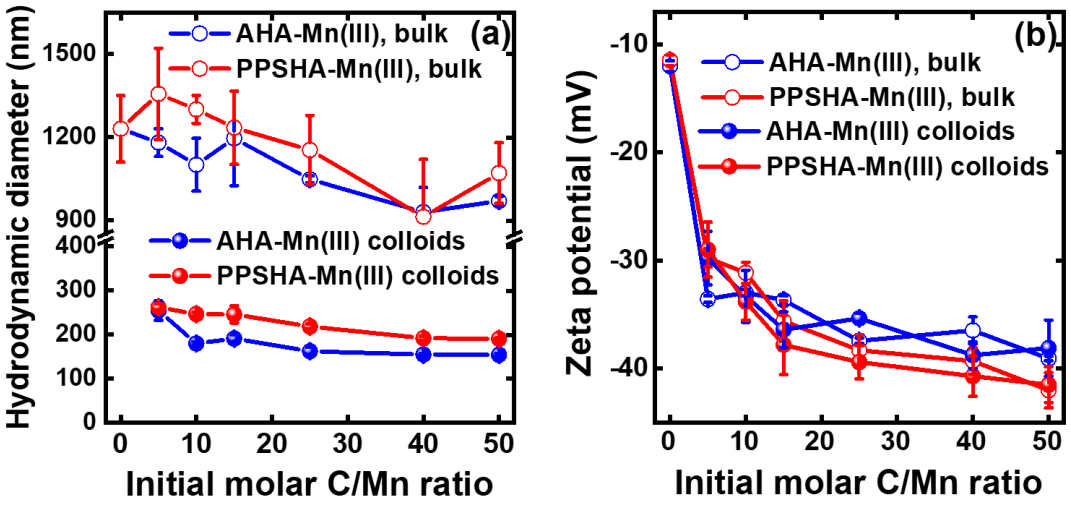

Fig. 3 (a) Z-averaged hydrodynamic diameter and (b) zeta potential of HA-Mn(III) colloids (1-3 to 450 nm) and larger particles in HA-Mn(III) suspensions (without any filtration treatments) at steady-state conditions as a function of initial C/Mn molar ratios. Each data refers to the mean of 10 measurements of duplicate samples. Error bars represent standard deviations.

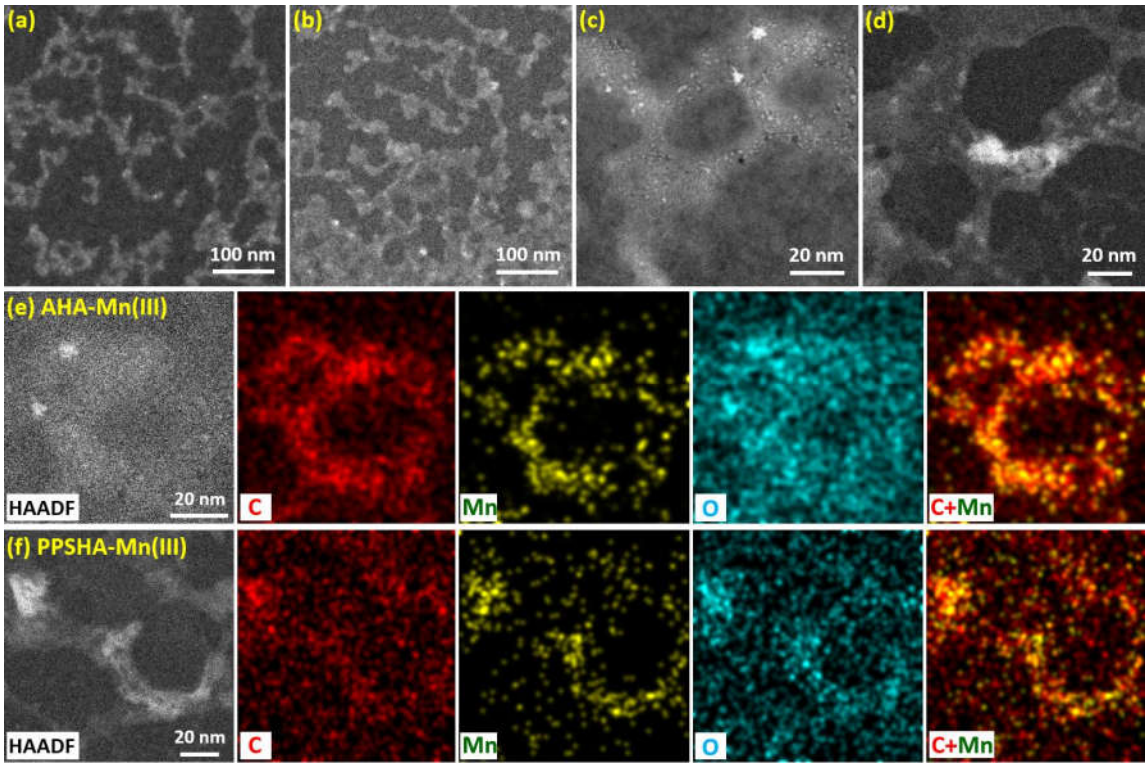

Fig. 4 Morphology and microscopic structure of HA-Mn(III) colloids. STEM images of (a,c) AHA-Mn(III) colloids and (b,d) PPSHA-Mn(III) colloids. HAADF images of (e) AHA-Mn(III) colloids and (f) PPSHA-Mn(III) colloids and the corresponding high-resolution EDS elemental mappings of C, Mn, and O, and color overlays of C and Mn. Both AHA-Mn(III) and PPSHA-Mn(III) colloids were imaged at an initial molar C/Mn ratio of 50.

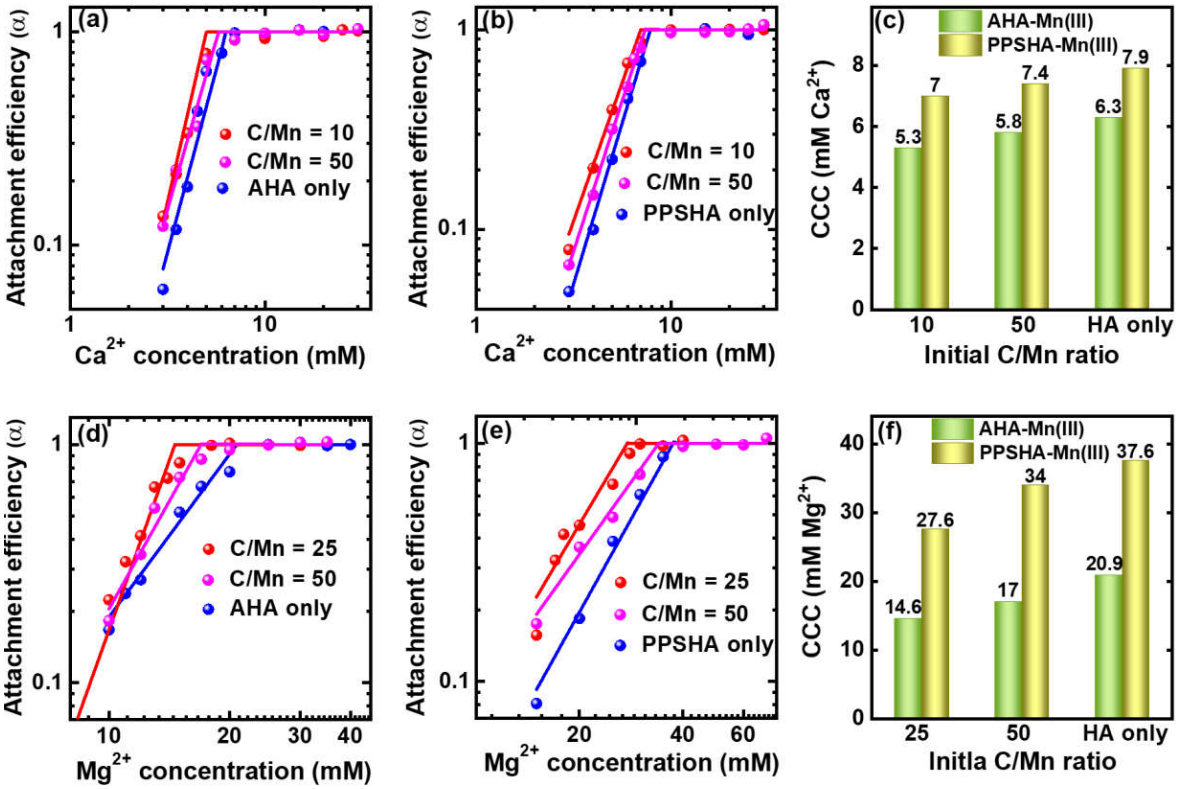

Fig. 5 Attachment efficiency of (a,d) AHA-Mn(III) colloids and (b,e) PPSHA-Mn(III) colloids for different C/Mn molar ratios as a function of concentrations of (a, b) Ca^{2+} and (d, e) Mg^{2+} at pH 7. The corresponding critical coagulation concentration (CCC), which was summarized in panels c and f, was derived by intersection of extrapolations through reaction-limited and diffusion-limited regimes as an index of particle aqueous stability.

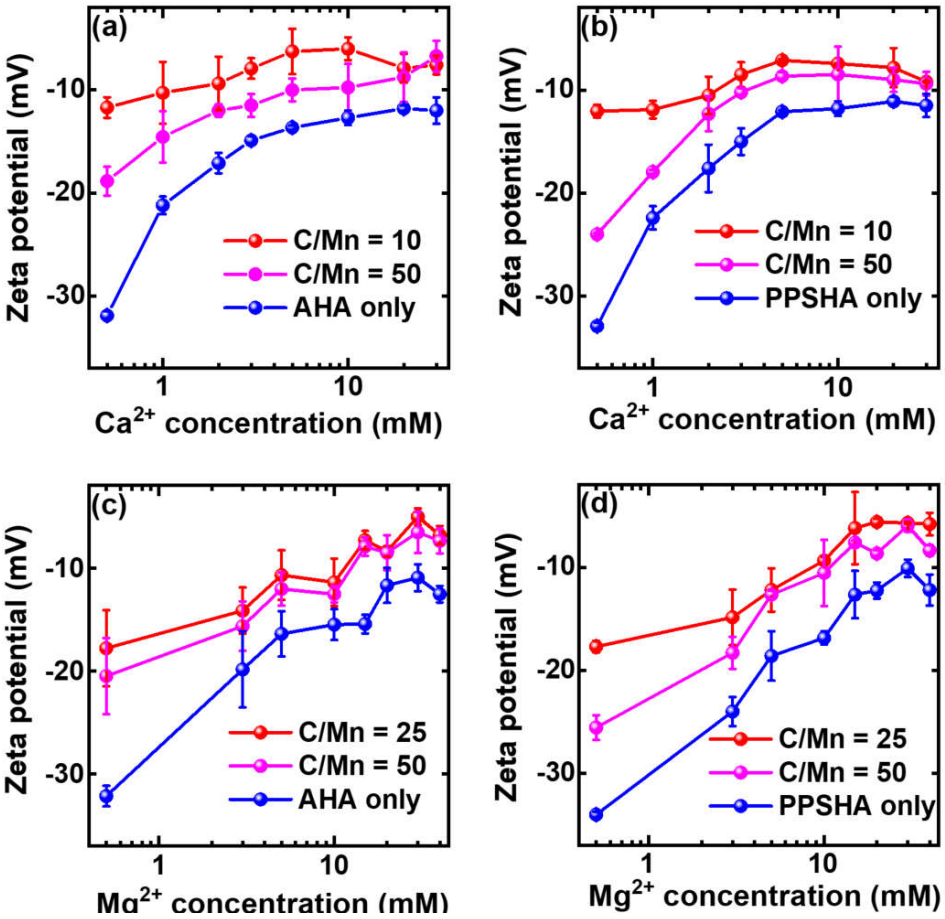

Fig. 6 Zeta potentials of different C/Mn molar ratios of (a,c) AHA-Mn(III) colloids and (b,d) PPSHA-Mn(III) colloids respectively over a range of (a, b) Ca^{2+} and (c, d) Mg^{2+} concentrations at pH 7. Each data point shows the mean of 10 measurements of duplicate samples. Error bars represent standard deviations.

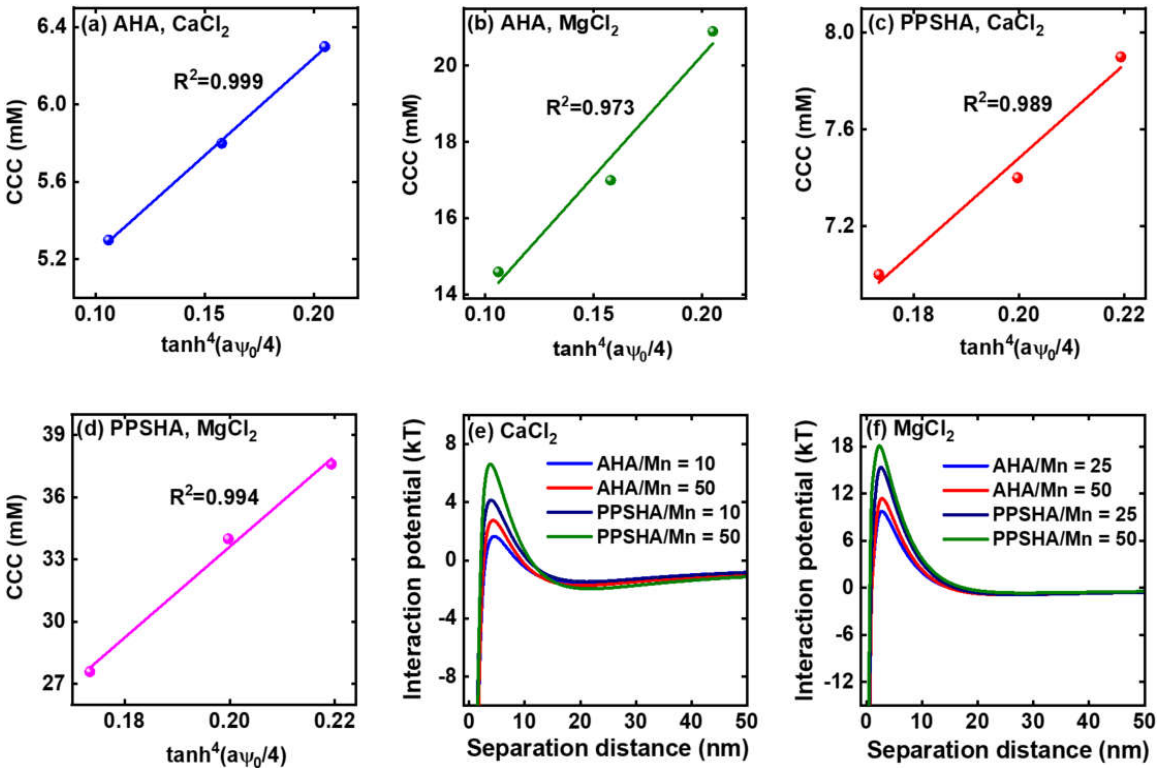

Fig. 7 (a-d) Correlation between the CCC values of HA-Mn(III) colloids and the zeta potentials. (e,f) Estimated total interaction energy as a function of separation distance using DLVO theory for HA-Mn(III) colloids at different initial molar C/Mn ratios in the presence of 1 mM (e) $CaCl_2$ and (f) $MgCl_2$.

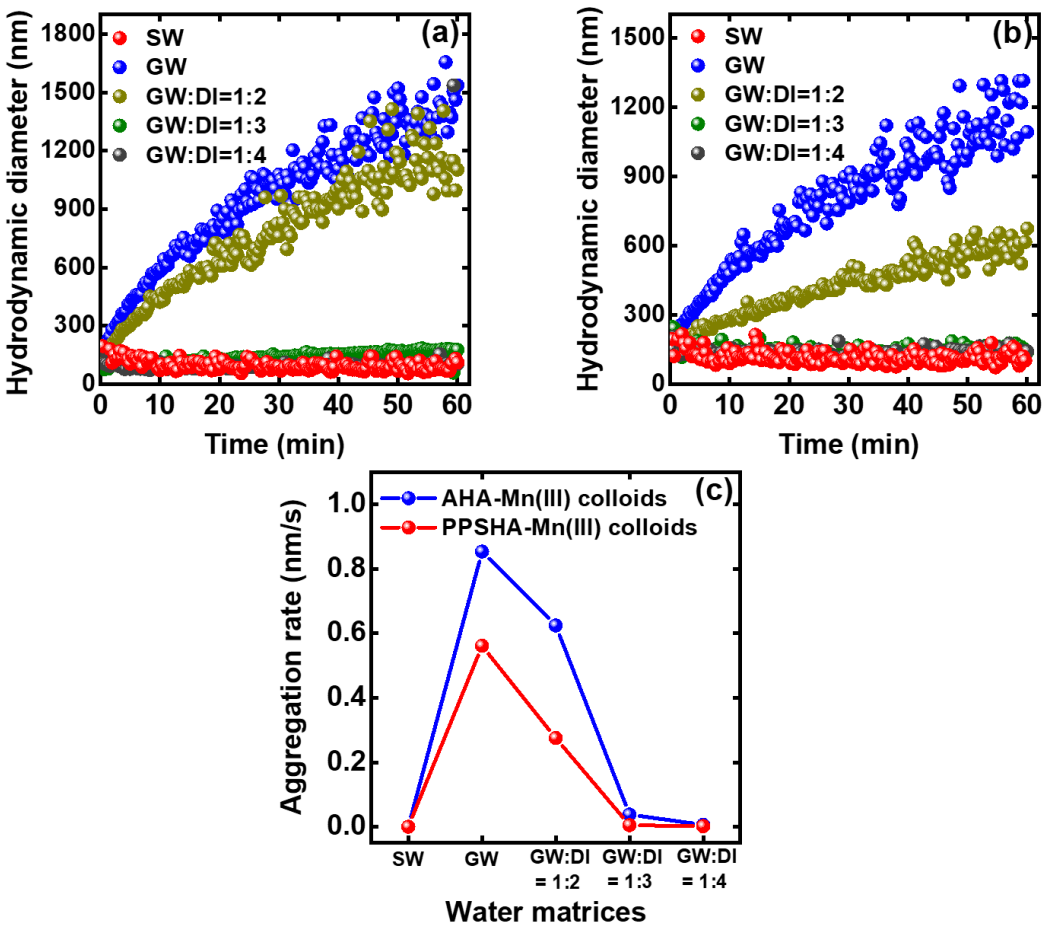

Fig. 8 The aggregation profiles of (a) AHA-Mn(III) colloids and (b) PPSHA-Mn(III) colloids, and (c) the corresponding initial aggregation rate in surface river water, groundwater, and groundwater with DI water for different mixtures. No appreciable aggregation was observed in the absence of HA-Mn(III) colloids, demonstrating that aggregation is due to the introduction of HA-Mn(III) colloids other than other impurities in waters. Aggregation rates were quantified from the initially linear increase in hydrodynamic diameter over time as described in section 2.3.